



Accuracy assessment of ASTER, SRTM, ALOS, and TDX DEMs for Hispaniola and implications for mapping vulnerability to coastal flooding

Keqi Zhang^{a,b,*}, Daniel Gann^c, Michael Ross^{a,d}, Quin Robertson^e, Juan Sarmiento^b, Sheyla Santana^c, Jamie Rhome^f, Cody Fritz^f

^a Department of Earth and Environment, Florida International University, Miami, FL 33199, USA

^b Extreme Events Institute, Florida International University, Miami, FL 33199, USA

^c GIS-Remote Sensing Center, Florida International University, Miami, FL 33199, USA

^d Southeast Environmental Research Center, Florida International University, Miami, FL 33199, USA

^e APTIM, Boca Raton, FL 33431, USA

^f National Hurricane Center, Storm Surge Unit, 11691 SW 17th St, Miami, FL 33165, USA

ARTICLE INFO

Keywords:

TanDEM-X
ASTER
SRTM
ALOS
LiDAR
RTK-GPS
DEM
Elevation accuracy
Coastal flood

ABSTRACT

Digital elevation models (DEMs) derived from remote sensing data provide a valuable and consistent data source for mapping coastal flooding at local and global scales. Mapping of flood risk requires quantification of the error in DEM elevations and its effect on delineation of flood zones. The ASTER, SRTM, ALOS, and TanDEM-X (TDX) DEMs for the island of Hispaniola were examined by comparing them with GPS and LiDAR measurements. The comparisons were based on a series of error measures including root mean square error (RMSE) and absolute error at 90% quantile (LE90). When compared with > 2000 GPS measurements with elevations below 7 m, RMSE and LE90 values for ASTER, SRTM, ALOS, TDX DEMs were 8.44 and 14.29, 3.82 and 5.85, 2.08 and 3.64, and 1.74 and 3.20 m, respectively. In contrast, RMSE and LE90 values for the same DEMs were 4.24 and 6.70, 4.81 and 7.16, 4.91 and 6.82, and 2.27 and 3.66 m when compared to DEMs from 150 km² LiDAR data, which included elevations as high as 20 m. The expanded area with LiDAR coverage included additional types of land surface, resulting in differences in error measures. Comparison of RMSEs indicated that the filtering of TDX DEMs using four methods improved the accuracy of the estimates of ground elevation by 20–43%. DTMs generated by interpolating the ground pixels from a progressive morphological filter, using an empirical Bayesian kriging method, produced an RMSE of 1.06 m and LE90 of 1.73 m when compared to GPS measurements, and an RMSE of 1.30 m and LE90 of 2.02 m when compared to LiDAR data. Differences in inundation areas based on TDX and LiDAR DTMs were between –13% and –4% for scenarios of 3, 5, 10, and 15 m water level rise, a much narrower range than inundation differences between ASTER, SRTM, ALOS and LiDAR. The TDX DEMs deliver high resolution global DEMs with unprecedented elevation accuracy, hence, it is recommended for mapping coastal flood risk zones on a global scale, as well as at a local scale in developing countries where data with higher accuracy are unavailable.

1. Introduction

Coastal zones are highly sought-after locations for residential, commercial, or tourism development because of an abundance of available resources and trading opportunities (McGranahan et al., 2007). Unfortunately, many coastal areas are characterized by low-relief topography only a few meters above sea level, and are constantly subjected to the impacts of wind, waves, currents, and tides (Komar, 1998). The concentration of population and economic activities in the

coastal zone exposes residents and infrastructure to an assortment of hazards, particularly flooding from storm surge in combination with high tides and overbank river flows. Sea level rise and variation in storm activity due to climatic change (Knutson et al., 2010; Nicholls et al., 2011) will increase the risk of flooding, threatening coastal residents. Therefore, it is critical to map areas likely to be flooded by storm surge and sea level rise, in order to inform policy-makers and the public about potential impacts on population, property, and infrastructure.

* Corresponding author at: Department of Earth and Environment, Florida International University, Miami, FL 33199, USA.

E-mail addresses: kzhang@fiu.edu (K. Zhang), gann@fiu.edu (D. Gann), rossm@fiu.edu (M. Ross), William.Robertson@aptim.com (Q. Robertson), jsarmien@fiu.edu (J. Sarmiento), shaguila@fiu.edu (S. Santana), jamie.r.rhyme@noaa.gov (J. Rhome), cody.fritz@noaa.gov (C. Fritz).

<https://doi.org/10.1016/j.rse.2019.02.028>

Received 5 November 2018; Received in revised form 2 February 2019; Accepted 28 February 2019

0034-4257/ © 2019 Published by Elsevier Inc.

The quality of mapping areas vulnerable to flooding relies upon the accuracy of a digital terrain model (DTM), which is often derived from airborne and satellite remote sensing. Methods employed to generate elevation data through remote sensing include optical stereo matching, radar interferometry, and light detection and ranging (LiDAR) (Takaku et al., 2014). DTMs with root-mean-square error (RMSE) as low as 0.10–0.15 m can be derived from airborne LiDAR remote sensing (Shan and Toth, 2008), and are often utilized to map coastal and freshwater flooding risk in developed countries. For example, Zhang (2011) and Zhang et al. (2011) used LiDAR DTMs to map potentially flooded areas, population, and property caused by sea level rise in South Florida in the United States (U.S.). However, LiDAR data are rarely available in developing countries because of the prohibitive cost and technical barriers to data collection and processing. Additionally, the development of coastal zones occurs on a global scale, thus a global DTM is needed to assess the cumulative effect of human activity on coastal flooding (McGranahan et al., 2007). Satellite based technology such as synthetic aperture radar (SAR) and stereo analysis of overlapping optical imagery offers a viable solution for collecting the elevations of the Earth's surface at a global scale.

Launched in 2000 by the U.S. National Aeronautics and Space Administration (NASA), the Shuttle Radar Topography Mission (SRTM) generated the first free global digital elevation model (DEM) for the lands between latitudes 60° N and 56° S (Farr et al., 2007). In 2009, the Ministry of Economy, Trade, and Industry (METI) of Japan and NASA released the Advanced Spaceborne Thermal Emission and Reflection Radiometer (ASTER) Global DEM for lands between 83° N and 83° S (Abrams et al., 2010; Tachikawa et al., 2011a), extending the coverage beyond that of SRTM. These two DEMs, especially the former, have been used to map potential flood areas on a global scale, and to document the population impacted by increased flooding due to sea level rise (Hinkel et al., 2014; McGranahan et al., 2007; Neumann et al., 2015). However, by comparing the areas of impacted land and population derived from LiDAR and SRTM data along the U.S. Coast, Kulp and Strauss (2016) demonstrated that errors in SRTM in low-lying areas resulted in a large underestimate of coastal vulnerability to sea level rise inundation. For example, for a flood level 2–3 m above the mean higher high water level, SRTM data under-predicted the inundated land areas and population by 50% and 60%, respectively.

Several studies have used SRTM and ASTER DEMs to depict the extent of inundation caused by sea level rise on a local scale (Demirkesen et al., 2008, 2007; Ho et al., 2010). However, sensitivity analysis of flood risk using LiDAR, SRTM, and ASTER DEMs for Lagos City, Nigeria showed that the flooded coastal areas estimated by ASTER and SRTM data were 3–10 times less than the flooded area from LiDAR (van de Sande et al., 2012). With the recent release of two global DEMs, the TanDEM-X (TDX) DEM by the German Aerospace Center (DLR) and the Advanced Land Observing Satellite (ALOS) World 3D DEM by the Japan Aerospace Exploration Agency (JAXA), more data are available for mapping the extent of flooding. The TDX mission specified the absolute vertical error at the 90% quantile (LE90) of the TDX DEM to be 10 m. However, a comparison of the TDX DEM with Ice, Cloud, and land Elevation Satellite (ICESat) laser altimeter measurements in areas not covered by ice or forest generated an LE90 error of only 0.88 m, which was much lower than the error specified by the mission (Rizzoli et al., 2017). Boulton and Stokes (2018) demonstrated that the ALOS DEM performance in geomorphological analysis of river networks within mountain landscapes was superior to those derived from SRTM, ASTER, or TDX DEMs. Recently, Gesch (2018) compared the vertical errors of SRTM, ASTER, ALOS, and TDX DEMs and examined their effect on mapping coastal inundation caused by sea level rise at seventeen sites along the U.S. coasts. However, to derive a general conclusion, more studies on the performance of these DEMs in depicting coastal inundation zones in different geographic areas need to be conducted. The questions of what effect DEM errors have on the delineation of flood areas, and which DEM data set is the best option for quantitative

analysis of flood risk caused by storm surge and sea level rise must be answered before TDX or ALOS DEMs are used to map coastal flood risk. Because high-accuracy LiDAR data are only available for limited coastal areas of Hispaniola, composed of Haiti and the Dominican Republic, the island is an ideal location to test the application of global DEMs for mapping the coastal flood zone. The objectives of this paper are therefore to (1) estimate the accuracy of SRTM, ASTER, ALOS, and TDX DEMs in low-lying coastal areas of Hispaniola by comparing DEMs with GPS and LiDAR measurements, (2) examine whether filtering methods for removal of buildings and trees can improve the generation of DTMs from TDX DEMs, and (3) assess the effect of elevation errors of DEMs on mapping coastal inundation areas, enabling the substitution of TDX DTMs for LiDAR DTMs in modeling coastal inundation to be evaluated.

2. Study area and data

2.1. Study area

Hispaniola is the second largest island in the Caribbean with an area of approximately 75,000 km² and a population of 22 million (United Nations, 2017). The topography is dominated by a series of mountains and intervening valleys oriented in the NW-SE direction, and elevations range from lake bottoms 40 m below sea level to mountains > 3000 m high (Rodriguez and Barba, 2009; Wilson et al., 2001). The island experiences frequent tropical cyclones due to its central location in the path of hurricanes that originate from West Africa and reach the Caribbean Sea. Historically, hurricanes have generated high storm surge and large waves along the coast of Hispaniola. Low-lying coastal areas such as Port-au-Prince, Gonaives, Cap-Haitien, Matancitas, Bebedero, San Pedro De Macoris, and Azua are vulnerable to storm surge flooding (Fig. 1). For example, during Hurricane David (1979) a 6 m storm tide (surge + wave setup + wave runup + tide) inundated most coastal highways from Santo Domingo to Las Americas International Airport, including the airport itself, threatening the lives of coastal residents and tourists (personal communication, Miguel Campusao, Oficina Nacional de Meteorología, The Dominican Republic).

2.2. SRTM DEM

NASA's void-filled SRTM DEM, with a resolution of 1 arc-second (~30 m at the Equator), was utilized in this study. SRTM DEMs are 16 bit signed integers, referenced horizontally to the World Geodetic System 1984 (WGS84) and vertically to the Earth Gravitational Model 1996 (EGM96). It is noteworthy that the C-band SAR was employed by the SRTM sensor to measure the height of ground and non-ground features across the Earth's surface. Since C-band wave cannot penetrate dense vegetation or buildings, SRTM DEMs represent elevations between the bare ground and canopy top. The accuracy of the 30 m SRTM DEM is specified as < 16 m absolute vertical elevation error and < 10 m relative vertical elevation error at the 90% confidence level (Farr et al., 2007). By comparing SRTM elevations with GPS measurements, Rodriguez et al. (2006) demonstrated that absolute elevation errors of SRTM at the 90% quantile ranged from 5.6 m to 9.0 m.

2.3. ASTER DEM

The ASTER DEM version 2 is a global one arc-second elevation dataset that was released in October 2011 by METI, Japan and NASA. The ASTER DEM was generated using optical imagery of 15 m resolution collected in space with the METI ASTER sensor mounted on NASA's Terra satellite (Abrams et al., 2010). Construction of the ASTER DEM relies on the correlation of stereoscopic image pairs (Wolf et al., 2000). Compared to ASTER DEM version 1, released in June 2009, the version 2 DEM improved spatial resolution, increased horizontal and vertical accuracy, and provided better water body coverage and detection by using 260,000 additional stereo-pairs (Tachikawa et al., 2011a). The

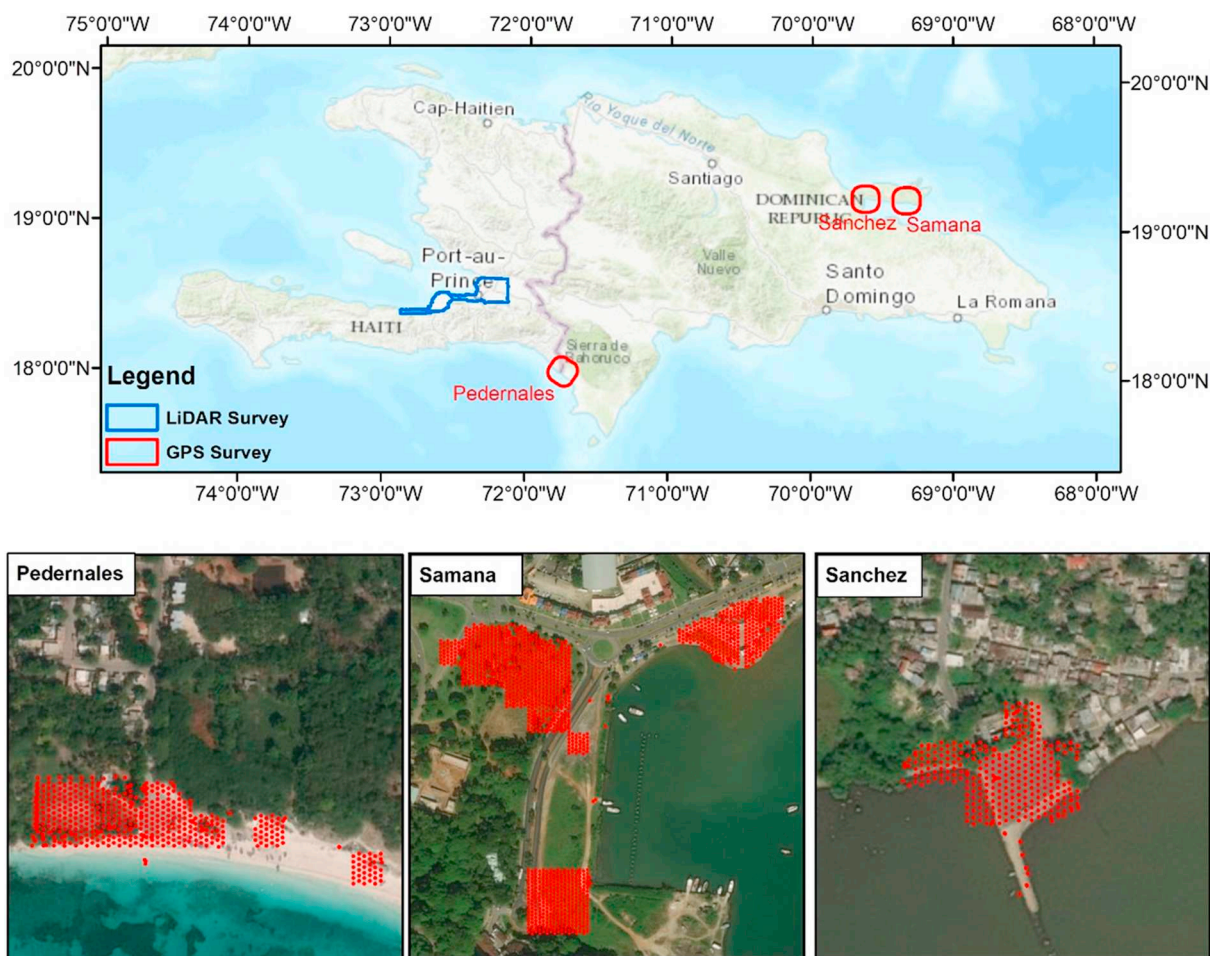


Fig. 1. Hispaniola and locations of GPS and LiDAR surveys.

elevations of ASTER DEMs are 16 bit signed integers, referenced horizontally to WGS84 and vertically to EGM96. During an observation period of more than seven years (2000–2007), about 1,260,000 scenes of stereoscopic DEM data sets, each covering an area of $60 \text{ km} \times 60 \text{ km}$, were collected, with the topography of most regions being sampled several times. The RMSE of ASTER elevations was estimated to be 8.68 m (Tachikawa et al., 2011b).

2.4. ALOS DEM

The ALOS was launched by JAXA in collaboration with commercial partners NTT DATA Corp. and the Remote Sensing Technology Centre of Japan (RESTEC) in 2013 (Tadono et al., 2014; Takaku et al., 2014). A Panchromatic Remote-sensing Instrument for Stereo Mapping (PRISM), an optical sensor on board of ALOS, was operated from 2006 to 2011, using PRISM stereo image pairs with a resolution of 2.5 m to generate a global DEM between latitudes 80° N and 80° S (Takaku and Tadono, 2009). NTT DATA and RESTEC have distributed fine resolution DEMs with an approximate 5 m pixel size commercially. JAXA generated $1^\circ \times 1^\circ$ tiles of 1 arc sec ($\sim 30 \text{ m}$) DEMs by resampling the 5 m ALOS DEMs, and released these products to the public in 2016 (Tadono et al., 2016). JAXA upgraded ALOS DEM to version 2.1 in 2017 (<http://www.eorc.jaxa.jp/ALOS/en/aw3d30/index.htm>, accessed 3 November 2018), filling in the elevations of water, low correlation, cloud, and snow pixels (Takaku and Tadono, 2017). Average and median elevations were produced for 30 m ALOS DEMs by averaging or selecting the median of the elevations of 49 (7×7) pixels of 5 m DEM elevations. The average DEM elevations used in this study are 16 bit signed integers, referenced to the WGS84 horizontal datum and EGM96 vertical

datum. Mean, standard deviation, and RMSE of ALOS DEMs versus 5121 control points distributed across 127 image tiles were -0.44 m , 4.38 m, 4.40 m, respectively (Takaku et al., 2016).

2.5. TDX DEM

The DLR, in partnership with private industry, launched the TDX DEM mission from 2010 to 2015 to generate a global DEM between latitudes 90° N and 90° S (Rizzoli et al., 2017; Wessel, 2016; Zink et al., 2014). The TDX twin X-band SAR sensors operated in a bistatic mode, utilizing a strip-map mode with a resolution of 3 m, a swath width of 30 km, and slant angles of 30° – 50° to derive elevations of the Earth's surface (Gruber et al., 2012; Krieger et al., 2007). The pixel spacing of the TDX DEM is 0.4 arc sec (about 12 m) in the latitudinal direction, and varies in the longitudinal direction from 0.4 arc sec at the equator to 4 arc sec above 85° N/S latitude (Wessel, 2016). The 32 bit float elevations of the TDX DEM were generated by averaging all SAR height values falling in a given pixel, using weights based on the standard deviations of the errors for these heights. The horizontal datum for the DEM is WGS84-G1150 and the heights of the DEM are ellipsoid heights referenced to WGS84-G1150 (Wessel, 2016). Comparison of TDX DEM elevations with kinematic GPS data derived by driving vehicles across all continents and elevations of GPS survey benchmarks covering the entire U.S. indicated that LE90s were 1.9 m for kinematic GPS and 2.0 m for GPS benchmarks, respectively (Wessel et al., 2018). Fifteen $1^\circ \times 1^\circ$ TDX DEM tiles that were collected from 2011 to 2014 cover the island of Hispaniola.

2.6. LiDAR data

In order to map the damage and fault movement due to a magnitude 7.0 earthquake that impacted Haiti in January 2010, LiDAR data were collected and processed by Rochester Institute of Technology under sub-contract to ImageCat Inc. (Van Aardt et al., 2011) (Fig. 1). The data collection effort was sponsored by the Global Facility for Disaster Reduction and Recovery hosted at The World Bank. The LiDAR surveys covered an 838 km² area around Port-au-Prince, Haiti, with a measurement density of 3.4 points per square meter. Three dimensional LiDAR data, reported in the horizontal WGS84 Universal Transverse Mercator (UTM) coordinate system and based on the EGM96 vertical datum, were distributed in binary LASer (LAS) format (<https://www.asprs.org/divisions-committees/lidar-division/laser-las-file-format-exchange-activities>, accessed 20 January 2019) and were downloaded from Open Topography (www.opentopography.org, accessed 3 November 2018). In the downloaded LAS dataset, the ground and non-ground LiDAR points were labeled with different class codes.

2.7. Ground GPS surveys

Real Time Kinematic Global Positioning System (RTK GPS) surveys were conducted in April 2016 at three sites within the Dominican Republic: Pedernales, Samana, and Sanchez, (Fig. 1). The survey points were determined using a systematic, staggered-start point sampling method (Franzen et al., 2011) within the square boundary of an SRTM grid cell to capture elevation changes within the cell. First, the sample locations started at the upper left vertex of the square grid cell and were planned at 0, 10, 20, and 30 m using a sample interval of 10 m along the *x* direction, thereby forming the first row of samples. Next, the *y* values of second row samples were derived by subtracting the *y* coordinates of first row samples by 5 m, and the sample locations were planned at 5, 15, and 25 m by alternating the starting position at half the sample interval along the *x* direction. Third, in addition to decreasing *y* values by 5 m along the *y* direction for each row, the third and fourth rows of *x* coordinates were planned in the same way as the first and second rows, respectively. This process was repeated until the *y* coordinates of the samples reached the bottom of the square boundary of the SRTM grid cell. The GPS data were collected by surveyors at locations within 10 cm circles around the predefined sampling points using rod-mounted RTK GPS rovers. If a sample point happened to be in an area with poor GPS reception during the survey, a point closest to the sample location was taken and labeled appropriately. This method was continued until all points at each site were completed, or until location conditions (trees, buildings, etc.) prevented further data collection.

For each sampling site, two control points were established for differential GPS correction, and simultaneous static GPS observations were recorded for a minimum of 8 h during the course of the surveys. The static GPS records for control points were processed utilizing the National Geodetic Survey Online Positioning User Service (OPUS) that created baselines from Continuously Operating Reference Stations (CORS). In total, 2287 GPS points were surveyed at three sites with horizontal coordinates in the WGS84 UTM Zone 19N system, and ellipsoidal heights relative to the International Terrestrial Reference Frame (ITRF) 2008 vertical datum.

3. Methods

3.1. Datum conversion

In order to make a consistent comparison of LiDAR and GPS surveys with SRTM, ASTER, ALOS, and TDX DEMs, all measurements must refer to the same horizontal coordinate system and vertical datum. Since there is no reliable local datum available for Hispaniola (Mugnier 2005), all data were converted to the WGS84 UTM Zone 19N coordinate system with a vertical datum of EGM2008 (Pavlis et al., 2012)

in units of meters using the National Geospatial Agency (NGA) Conversion tool (http://earth-info.nga.mil/GandG/wgs84/gravitymod/egm2008/egm08_wgs84.html, accessed 3 November 2018) and the ArcGIS Projection tool. For SRTM, ASTER, and ALOS DEMs, the horizontal and vertical coordinates of each grid cell referenced to WGS84 and EGM96, respectively, were first output as a text file. Elevations were then transformed to ellipsoid heights relative to WGS84, and to heights with respect to EGM2008 using the NGA Conversion tool. Finally, the EGM2008 heights in ASCII format were converted to raster in ArcGIS and projected to the UTM coordinate system. TDX DEMs with horizontal coordinates and ellipsoid heights relative to WGS84 were converted to the UTM coordinate system with a vertical datum of EGM2008 through steps 2 and 3 outlined above. For LiDAR data in the UTM coordinate system with a vertical EGM96 datum, the 12 m and 30 m digital surface models (DSMs) were first generated by simply averaging first return points in a grid cell using the LAS Dataset to Raster tool in ArcGIS. This reduced computation time, which was critical because the averaging process involved about 2.8 billion points (about 3.4 points per square meters), while guaranteeing the quality of DSMs. The 12 m and 30 m DTMs were generated by inverse distance weighted interpolation of ground LiDAR points to compute the elevations of grid cells occupied by buildings and vegetation. The DSMs and DTMs were then transformed to the WGS84 coordinate system in ArcGIS and converted to the UTM coordinate system with the EGM2008 vertical datum, following the same procedure as used to transform SRTM DEMs. The ellipsoid heights of the GPS measurements in reference to ITRF 2008 were converted to EGM2008 heights using the NGA Conversion tool for transforming WGS84 ellipsoid heights to EGM2008 heights, because the ITRF2008 and WGS84 ellipsoid heights coincided to approximately the 10 cm level (ITRF, 2013).

3.2. Generation of TDX DTMs by filtering and interpolation

The SRTM, ASTER, ALOS, and TDX DEMs include canopy and building measurements because electronic and magnetic waves recorded by radar or optical sensors cannot penetrate fully through vegetation and buildings to reach the ground. Hence, the SRTM, ASTER, ALOS, and TDX DEMs actually represent DSMs that include the elevations of non-ground features. The terms DEM and DSM were used interchangeably in this study to keep the DEM terminology used by many agencies providing the data. To improve the accuracy of mapping storm surge flooding using these DEMs, non-ground elevations must be removed, especially in low-relief coastal areas. Because of their coarse horizontal (30 m) and vertical resolutions (1 m), this is a challenging task with SRTM, ASTER, and ALOS DEMs. However, the higher spatial and vertical resolutions of the TDX DEM make it possible to remove vegetation and building elevations based on elevation changes within a neighborhood (local window) (Geiß et al., 2015). We used four filtering methods for airborne LiDAR data, including the elevation threshold with expanding window (ETEWE) filter, the progressive morphological filter with one dimensional (PM) or two dimensional (PM2D) structure elements, and the adaptive triangulated irregular network (ATIN) filter (Axelsson, 2000; Cui et al., 2013; Zhang, 2007; Zhang et al., 2003; Zhang and Whitman, 2005) to remove non-ground pixels in TDX DEMs. The horizontal (*x* and *y*) and vertical (*z*) coordinates of LiDAR points are used by these filters to generate ground measurements. Thus, prior to filtering, TDX DEMs were converted into points based on the horizontal coordinates and elevations of grid cells using Python (www.python.org). The parameters for the ETEWE method included an initial square window size of 10 m, a slope of 0.07, a window series of 1, 2, 4, 8, and 16 cells for five iterations, and height difference thresholds of 1.4, 2.8, 5.6, 11.2, and 22.4 m corresponding to the window series. The parameters for the ATIN method employed an initial square window size of 200 m, a height difference threshold of 0.4 m, and an angle threshold of 3°. For embarrassingly parallel computation, the dataset was subdivided into 2000 m × 2000 m tiles with overlap buffers of

200 m. The PM method used a cell size of 10 m, a window series of 1, 2, 4, and 8 cells, and height difference thresholds of 0.25, 0.5, 1.1, and 1.2 m corresponding to the window series without rotation of raw data. The PM2D method used a cell size of 10 m, a window series of 10, 20, 30, and 40 cells, and height difference thresholds of 3, 6, 12, and 18 m corresponding to the window series without rotation of the raw data. The details of these filtering parameters can be found in Zhang (2007) and Zhang and Whitman (2005).

The DTMs were generated by interpolating the ground pixels of the filtered TDX DEMs, using Empirical Bayesian Kriging (EBK) in ArcGIS. The EBK method was selected for the interpolation because (1) EBK has the ability to smooth out the outliers in the filtered pixels, and (2) the parameters used by EBK are automatically optimized by sub-setting the large dataset and using a spectrum of semivariograms generated through an iterative simulation process, instead of using a single semivariogram as in traditional kriging methods (Krivoruchko, 2012; Mirzaei and Sakizadeh, 2016; Roberts et al., 2014). The semivariogram that quantifies the spatial dependence in the filtered pixels is a function of the distance and direction separating pairs of pixels.

3.3. Elevation accuracy analysis

The vertical errors of the DEMs were quantified by comparing individual test DEM elevations (y_i) and reference LiDAR or GPS elevations (x_i) at sample points (i) using the following metrics (Davis, 2002; Höhle and Höhle, 2009; Wessel et al., 2018):

$$\text{Mean Error: } ME = \frac{1}{N} \sum_{i=1}^N (y_i - x_i) = \frac{1}{N} \sum_{i=1}^N \Delta h_i \tag{1}$$

$$\text{Mean Normalized Bias: } MNB = \frac{1}{N} \sum_{i=1}^N \frac{\Delta h_i}{x_i} \cdot 100\% \tag{2}$$

$$\text{Root Mean Square Error: } RMSE = \sqrt{\frac{1}{N} \sum_{i=1}^N \Delta h_i^2} \tag{3}$$

$$\text{Standard Deviation: } SD = \sqrt{\frac{1}{N-1} \sum_{i=1}^N (\Delta h_i - ME)^2} \tag{4}$$

$$\text{Median (50\% quantile): } MD = Q_{\Delta h}(0.5) = m_{\Delta h} \tag{5}$$

$$\text{Normalized Median Absolute Deviation: } NMAD = 1.4826 \cdot \text{median}(|\Delta h_i - m_{\Delta h}|) \tag{6}$$

$$\text{Absolute error at the 90\% quantile: } LE90 = Q_{|\Delta h|}(0.9) \tag{7}$$

where Δh_i is the difference between y_i and x_i and N is the total number of samples. NMAD is a nonparametric estimate for SD and is equal to SD if the difference follows a normal distribution.

The linear regression:

$$y_i = a + bx_i + \varepsilon_i \tag{8}$$

where ε_i is the random error following a normal distribution. The R-squared value of the linear regression equation was calculated by

$$R^2 = \frac{\sum_{i=1}^N (a + bx_i - y_m)^2}{\sum_{i=1}^N (y_i - y_m)^2} \tag{9}$$

where y_m is the mean of y_i . The p-value, that is the two-sided probability value of the null hypothesis that the slope of the regression equation is zero (Davis, 2002), was employed to examine the significance of the regression parameter. A low p-value (e.g., < 0.01) indicates that the null hypothesis may be rejected.

For accuracy analysis based on LiDAR measurements, these error measures were calculated using elevation pairs from 30 m ASTER, SRTM, and ALOS DEMs versus 30 m LiDAR DSMs, and elevation pairs from 12 m TDX DEMs and DTMs versus 12 m LiDAR DSMs and DTMs,

respectively, for overlapping areas. For accuracy analysis based on GPS measurements, the mean and standard deviation of the GPS elevations within a 30 m grid cell of ASTER, SRTM, and ALOS DEMs, or within a 12 m grid cell of TDX DEMs and DTMs in the overlapping area were calculated. Error measures were then calculated using elevation pairs from 30 m DEMs versus mean values of associated GPS measurements, and elevation pairs from 12 m DEMs and DTMs versus associated mean values of GPS measurements. If the number of GPS points within a grid cell was less than five, the grid cell and associated GPS measurements were excluded from comparison to ensure sufficient samples within a grid cell.

3.4. Delineation of potential flood area

The height of short-term floods caused by tides, storm surges and wave runups reaches about 10 m for Category 5 hurricanes, based on preliminary numerical modeling by the Storm Surge Unit at the National Hurricane Center. The potential long-term flood height at the end of the 21st century caused by the worst sea level rise scenario was estimated to be about 2–3 m (Bamber et al., 2009; Sweet et al., 2017). Therefore, the flood risk along the Hispaniola coast from the combination of tides, storm surges, wave runups, and sea level rise were categorized into high (locations at 0–3 m elevation), moderate (3–5 m elevation), low (5–10 m elevation), and extremely low (10–15 m elevation) risk categories. Since the inundated area for a rise of h in water level is equivalent to the coastal area below elevation h but above current sea level (EGM2008) if both sea level and elevation are referenced to the same vertical datum, flood risk areas corresponding to these categories were derived using a polygon formed by the shoreline and the contours corresponding to elevation h , following the procedure developed by Zhang et al. (2011).

In estimating the uncertainty of the flood risk maps generated using DTMs, it is important to quantify the horizontal position error of contour lines caused by vertical elevation uncertainty. The horizontal errors from TDX DTMs were examined by comparing the TDX and LiDAR contour lines in the same area, following a procedure used to map shoreline and beach volume change (Leatherman and Clow, 1983; Robertson et al., 2018; Zhang and Robertson, 2001). First, an offshore baseline that was approximately parallel to the contour lines was created in ArcGIS. Second, transects perpendicular to the baseline at a given interval (e.g., 100 m) were generated. Third, the distances between the contour lines and the baseline along transects were calculated to derive the differences between TDX and LiDAR contour lines (Fig. 2a).

The derivation of contour line position errors by comparing TDX and LiDAR contours only works for areas where both data sets exist. This method cannot be applied in areas where LiDAR data are not available. An alternative is to apply the elevation error derived by a comparison between TDX and LiDAR DTMs in overlapping coastal areas to the remaining coastal areas in Hispaniola, under the assumption that the elevation error of the remaining area is the same as the error in the overlapping area. Given a TDX contour (y_c), the systematic offset (m), the random error (σ) of the differences between TDX (y_i) and LiDAR DTM (x_i) elevations, and the vertical error (δ) of LiDAR measurements, the lower (h_l) and upper (h_u) boundaries of the true contour (h_c) are estimated by:

$$\begin{aligned} h_l &= y_c + m - \sigma - c\delta \\ h_u &= y_c + m + \sigma + c\delta \end{aligned} \tag{10}$$

where parameters σ and δ are independent, c is a constant (e.g., 2 or 3), and σ can be estimated by SD, RMSE, NAMD, or LE90. A quality check for LiDAR data in the study area is not available. Since the RMSE error of an airborne LiDAR survey is usually lower than 0.15 m (Shan and Toth, 2008), δ was set to be 0.15 m in this study. The flood zone and associated zones of uncertainty were estimated by the inundated areas

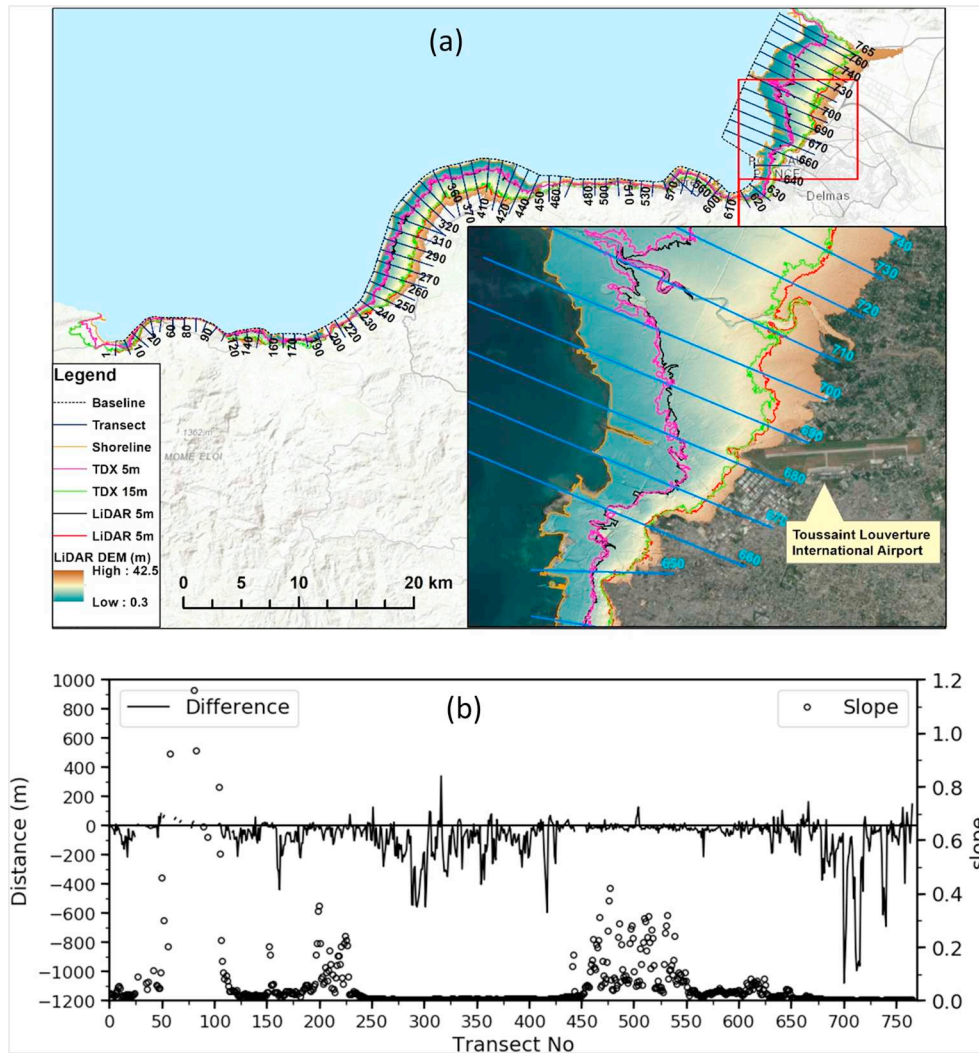


Fig. 2. (a) Baseline, transects across the shoreline, and contours. The interval between two adjacent transects is 100 m and for clarity only one of ten consecutive transects is displayed. The shoreline section around Toussaint Louverture International Airport is enlarged in the imbedded map. (b) The differences between 5 m contours from LiDAR and TDX DTMs along transects. Large contour line differences occur between transects 700 and 720, a marsh area next to the river on the delta plain.

between the shoreline and h_i , h , and h_u contours from TDX DTMs, given a rise of h in water level.

4. Results

4.1. Satellite DEMs and DTMs versus GPS measurements

Comparison of GPS measurements at Pedernales, Samana, and Sanchez with ASTER DEMs indicated that ME was about 4.83 m and MNB reached 654.4% (Table 1). It is noteworthy that MNB is sensitive to elevation differences at low elevations, and overestimates or underestimates indicated by MNB are not bounded by 100% as indicated by Eq. (2). The ASTER DEM elevations were scattered between about 0 to 22 m while GPS elevations varied from 0 to 4 m (Fig. 3), which implied that ASTER DEM elevations largely overestimated the topographic elevations at the three locations, resulting in the large SD of 6.96 m, RMSE of 8.44 m, and LE90 of 14.29 m. Compared to the ASTER DEM elevations, the scatter of SRTM elevations versus GPS elevations was reduced, but still quite large, generating an ME of 2.83 m and MNB of 277.0%. SD, RMSE, and LE90 of SRTM elevations were 2.58, 3.82, and 5.85 m, respectively, less than half of ASTER's values. SD, RMSE, and LE90 of ALOS elevations were further reduced to 1.87, 2.08, and

3.64 m, respectively. These values together with a smaller ME of 0.92 m and an MNB of 90.8% implied that ALOS elevations approximated Earth's surface elevations better than ASTER and SRTM at the three sites. With the smallest ME of 0.71 m and MNB of 39.4% in combination with the smallest SD of 1.59 m, RMSE of 1.74 m, and LE90 of 3.20 m, TDX DEM elevations estimated surface elevations best among the four data sources.

More TDX versus GPS elevation points were above the 1:1 line than below it, indicating that there was an offset of TDX elevations (Fig. 3). This offset existed because the TDX DEMs includes the elevations of non-ground pixels. Therefore, it is necessary to remove non-ground pixels from TDX DEMs to produce DTMs. The DTMs derived by filtering TDX DEMs using the ETEW, ATIN, PM, and PM 2D methods and interpolating identified ground pixels generated a smaller set of SD, RMSE, and LE90 values in comparison with values for the unfiltered TDX DEM (Table 1). The scatter plots for DTM versus GPS elevations showed that the ETEW and PM methods produced less scatter among data points in comparison with the ATIN and PM2D methods (Fig. 4). The DTM derived from the PM method generated the smallest SD of 1.03 m, RMSE of 1.06 m, and LE90 of 1.73 m among four DTMs.

ASTER, SRTM, ALOS, and unfiltered TDX DEMs, and TDX DTMs were compared with GPS measurements along a profile at Samana to

Table 1

Error measures. The representative row in the table is explained as follows. The row of “ASTER:GPS” shows the error measures of the differences between ASTER elevations and mean GPS elevations within ASTER grid cells. The row of “ETEWE:GPS” shows the error measures of the differences between the elevations of the ETEWE filtered TDX DEM and mean GPS elevations within TDX grid cells. The row of “ASTER:LiDAR” shows the error measures of the differences between the ASTER and LiDAR elevations. The row of “ETEWE:LiDAR” shows the error measures of the differences between the filtered TDX DEM and LiDAR DTM elevations. The row of “PM:LiDAR 3 m” shows the error measures of the differences between 3 m contours from the PM filtered TDX DEM and LiDAR DTM.

Comparison	Number of samples	ME (m)	MD (m)	MNB (%)	SD (m)	RMSE (m)	NMAD (m)	LE90 (m)	R ²
ASTER:GPS	95	4.83	3.01	654.4	6.96	8.44	8.33	14.29	0.31
SRTM:GPS	95	2.83	3.00	277.0	2.58	3.82	2.29	5.85	0.00
ALOS:GPS	95	0.92	0.20	90.8	1.87	2.08	1.63	3.64	0.10
TDX:GPS	125	0.71	0.23	39.4	1.59	1.74	0.99	3.20	0.32
ETEWE:GPS	125	-0.09	-0.16	-11.3	1.14	1.14	1.21	1.81	0.69
ATIN:GPS	125	0.28	0.08	4.1	1.37	1.39	1.19	2.15	0.62
PM:GPS	125	-0.27	-0.22	-20.2	1.03	1.06	1.06	1.73	0.74
PM2D:GPS	125	0.33	0.10	7.2	1.33	1.37	1.17	2.24	0.61
ASTER:LiDAR	165,624	2.45	2.41	94.5	3.46	4.24	3.42	6.70	0.66
SRTM:LiDAR	165,624	4.18	3.95	89.6	2.38	4.81	2.09	7.16	0.87
ALOS:LiDAR	165,624	4.46	4.17	97.5	2.06	4.91	1.52	6.82	0.90
TDX:LiDAR	1,022,699	1.27	0.69	20.0	1.88	2.27	1.12	3.66	0.92
ETEWE:LiDAR	1,022,699	0.76	0.57	12.5	1.47	1.66	0.96	2.51	0.94
ATIN:LiDAR	1,022,699	0.80	0.59	12.8	1.32	1.55	0.94	2.29	0.95
PM:LiDAR	1,022,699	0.60	0.40	8.5	1.16	1.30	0.81	2.02	0.96
PM2D:LiDAR	1,022,699	0.88	0.63	14.3	1.33	1.60	1.03	2.57	0.95
PM:LiDAR 3 m	694	-49.2	-20.9	-5.8	104.4	115.3	52.9	172.9	0.99
PM:LiDAR 5 m	709	-75.0	-28.4	-6.5	144.5	162.7	48.7	211.1	0.99
PM:LiDAR 10 m	720	-59.9	-26.0	-3.3	123.0	136.7	51.4	202.9	1.00
PM:LiDAR 15 m	711	-66.4	-29.8	-1.7	115.5	133.2	56.9	232.8	1.00

illustrate the spatial variation in the differences between satellite and GPS based elevations (Fig. 5). Between the distances of 0–250 m from shore to inland along the profile, ASTER elevations were much higher than GPS elevations and the lowest ASTER elevation at 145 m along the profile differed by about 4 m from the GPS elevations. Hence, the

application of filter methods to ASTER DEMs would not improve the estimates much because of large errors in DEM elevations and coarse horizontal and vertical resolutions. SRTM and ALOS DEM elevations along the profile were closer to GPS elevations, outperforming ASTER DEMs. However, over- or underestimates of topographic elevations

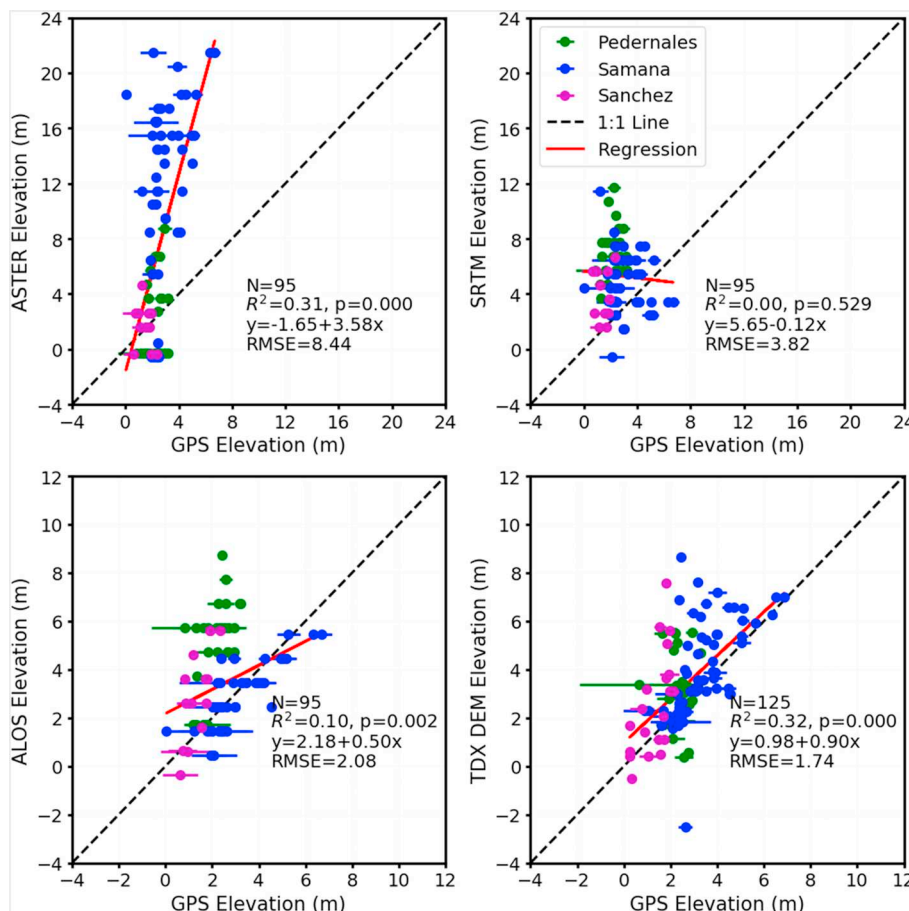


Fig. 3. Scatter plots of ASTER, SRTM, ALOS, and TDX DEM elevations versus GPS measurements at Pedernales, Samana, and Sanchez in the Dominican Republic. The value of GPS elevation and horizontal bar of a data point represents the mean and standard deviation of the GPS elevations within a DEM grid cell. Note that the ranges of ALOS and TDX DEM elevations are reduced by half of the ranges of ASTER and SRTM elevations to show elevation scatteredness better.

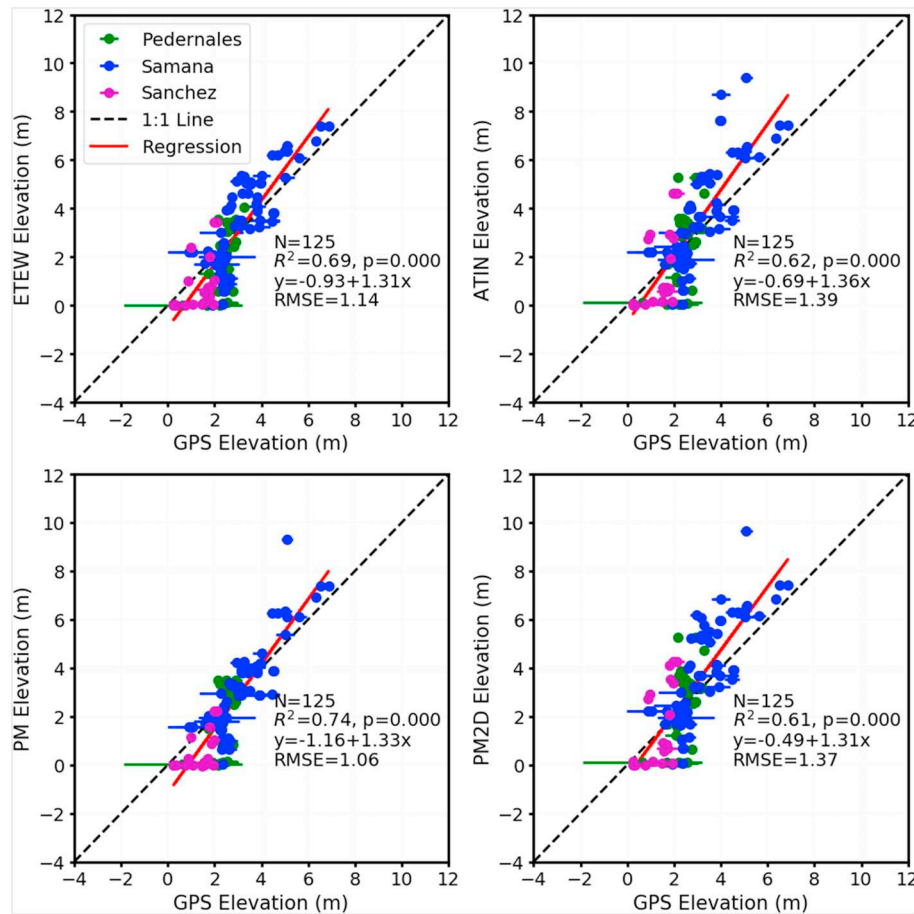


Fig. 4. Scatter plots of DTM elevations from the EWE, ATIN, PM, and PM2D filters versus GPS measurements at Pedernales, Samana, and Sanchez in the Dominican Republic.

ranging from 2 to 4 m by SRTM and ALOS were observed along the profile. The TDX DTMs generated by the PM and EWE methods were closest to GPS measurements between the distances of 0–250 m along the profile. Note that the elevation change caused by a small pit adjacent to the shoreline as indicated by GPS measurements was not captured by any of the four DEMs.

4.2. Satellite DEMs and DTMs versus LiDAR measurements

Comparison of satellite DEMs and DTMs with GPS measurements in three areas adjacent to the shoreline illustrated error measures below 7 m elevation (Figs. 3 and 4). Although the accuracy of kinematic GPS data as the reference was high, the coverage of spatial variation in topography was limited because of the intensive labor and high costs required to obtain GPS measurements compared to a remote sensing method. Hence, the LiDAR measurements covering 76 km of shoreline and 150 km² coastal areas were used to further examine the accuracy of satellite DEMs. Only pixels below the 20 m contour of the LiDAR DTM were used to conduct the comparisons, because even the most aggressive estimate of the potential coastal flooding caused by storm surge and sea level rise within 100 years does not exceed this height.

ASTER DEM generated the largest SD of 3.46 m (Table 1), which is consistent with the distribution of elevation differences between ASTER and LiDAR (Fig. 6a) and the relatively large scatter of data points for ASTER versus LiDAR elevations (Fig. 7). However, ME, RMSE, and LE90 of ASTER were smaller than those of SRTM and ALOS (Table 1) because of large positive offsets of SRTM and ALOS elevations from LiDAR elevations (Fig. 7). The Q-Q plot showed that the distribution for elevation differences between ASTER and LiDAR approximated a normal

distribution (Fig. 6b), therefore, the values of SD and NAMD were almost the same (Table 1). TDX DEM elevations produced the least scatter (Fig. 7) among the four satellite data sets, leading to the smallest SD of 1.88 m, RMSE of 2.27 m, and LE90 of 3.66 m. The scatter plot for TDX versus LiDAR in Fig. 7 exhibited a positive offset and the histogram for the difference between TDX and LiDAR DEM elevations showed a severe skewness toward the positive value (Fig. 6a), far from the normal distribution as indicated by the Q-Q plot (Fig. 6e). The differences of SRTM and ALOS elevations versus LiDAR elevations showed less scatter and lower similarity to a normal distribution than ASTER versus LiDAR (Fig. 6c and d), but a much higher similarity than TDX versus LiDAR.

The error measures for the differences between LiDAR and TDX DTM elevations indicated that the EWE, ATIN, PM, and PM2D methods improved the accuracy of TDX elevations (Table 1). The PM filter generated the best result, with a SD of 1.16 m, RMSE of 1.30 m, and LE90 of 2.02 m, representing a 43% reduction in vertical error compared to the unfiltered TDX elevation data in terms of RMSEs. The ME and MNB of the DTM from the PM filter method were 0.60 m and 8.5%, a 53% drop in ME and 57% drop in MNB; this indicated that a large portion of the offset error in unfiltered TDX DEMs was removed by the filter. The scatter plots for the PM-based DTM elevations versus LiDAR elevations also showed that the offset of the unfiltered TDX DEMs with elevations below 15 m was removed (Fig. 8). Although EWE, ATIN, and PM2D produced larger SD, RMSE, and LE90 values, these three filters also removed most of the offset below 15 m (Fig. 8). An under-filtering of non-ground features at higher elevations was evident in Fig. 9, which displays elevation variations of unfiltered and filtered TDX data along a profile near Port-au-Prince. The dense trees and buildings on the land surface above 12 m were largely removed by

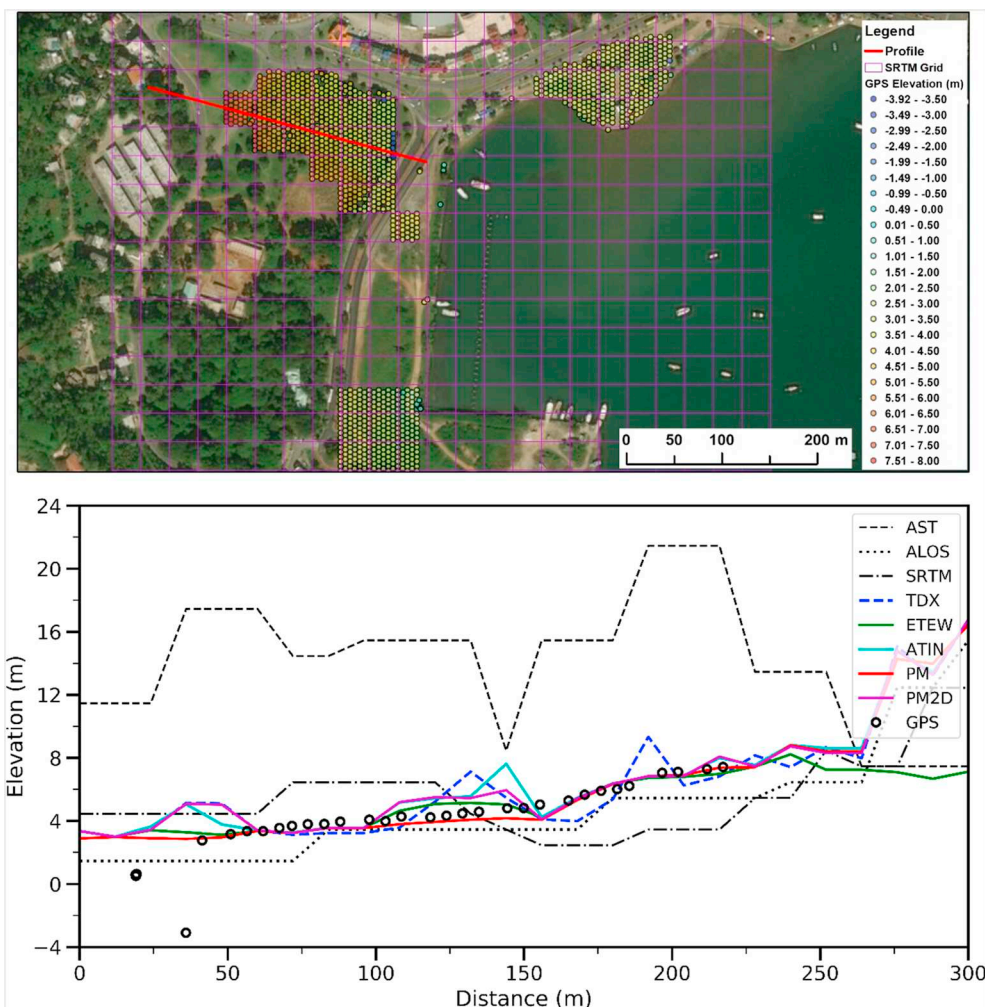


Fig. 5. The aerial photograph, GPS points, grid cells of the SRTM DEM (upper panel), and the elevation profile across the GPS measurements (lower panel) at Samana in the Dominican Republic. The GPS measurements along the profile were generated by projecting the points within a 100 m buffer zone to the profile line. The x coordinate of the profile starts from shore (zero) and extends inland (left side of the aerial photograph).

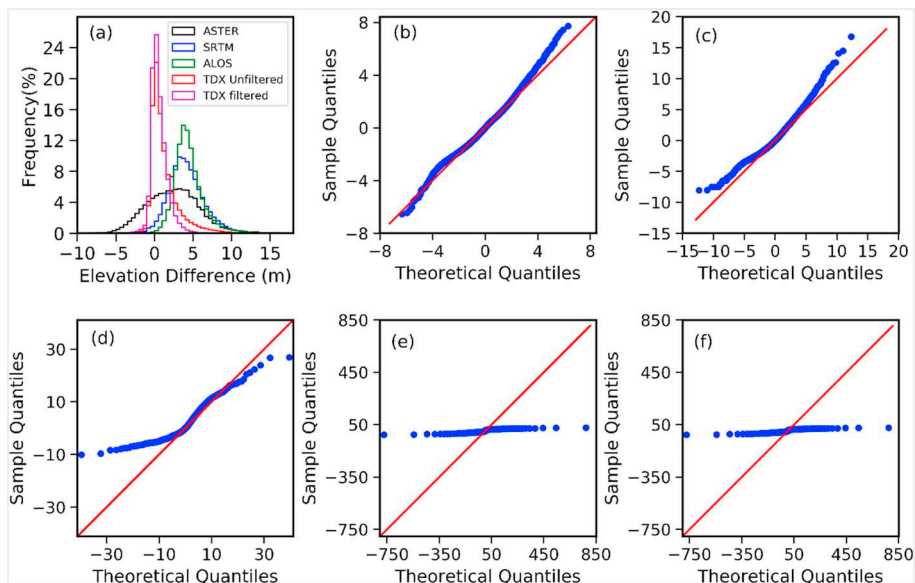


Fig. 6. (a) The distribution of the elevation differences between the ASTER DEM, SRTM DEM, ALOS DEM, TDX DEMs, PM based DTM, and LiDAR DTM. Q-Q plots for the differences between (b) ASTER and LiDAR, (c) SRTM and LiDAR, (d) ALOS and LiDAR, (e) TDX and LiDAR, and (f) PM based TDX and LiDAR elevations.

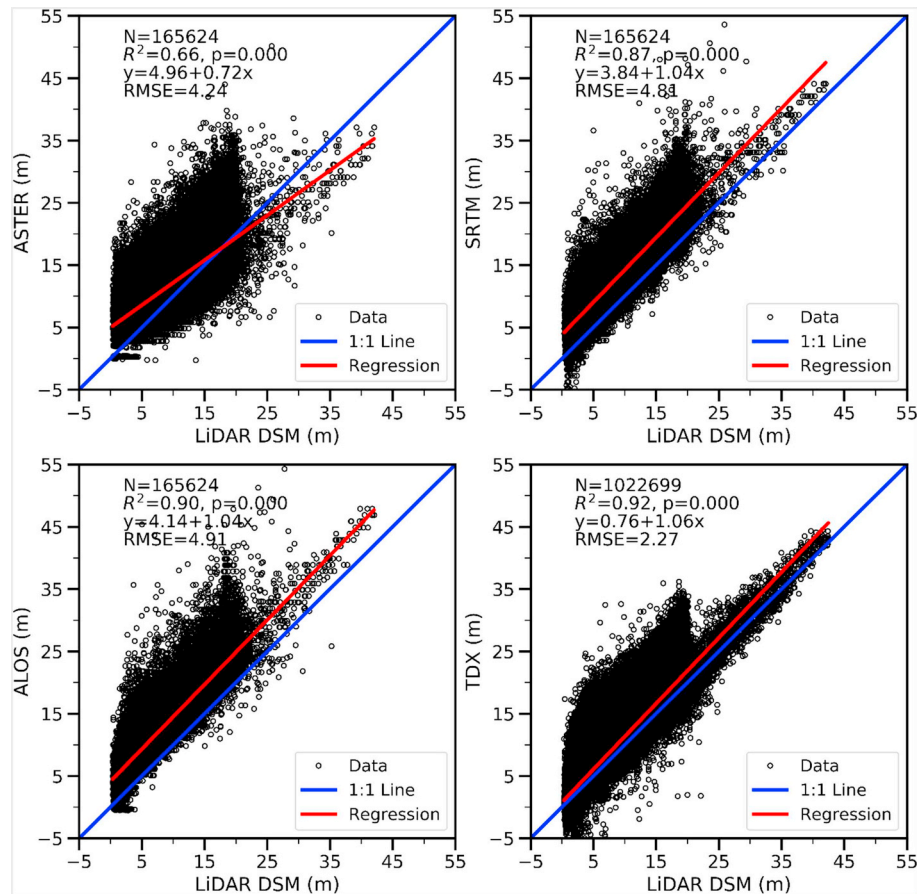


Fig. 7. Scatter plots of ASTER, SRTM, ALOS, and TDX DEM elevations versus the LiDAR DSM elevations around Port-au-Prince in Haiti.

the filters, but there were varied offsets between TDX and LiDAR DTMs. The major challenge here was that the pixels of TDX DEMs did not reach the ground over a large portion of the profile with higher elevations. For example, the TDX DEM data did not capture ground elevations between the distances of 4400 and 5000 m as indicated by unfiltered TDX and LiDAR elevations in Fig. 9, making it difficult for the filters to derive ground elevations within this interval. It is also noteworthy that ASTER, SRTM, and ALOS elevations largely over-estimated the ground elevations under 8 m even though there were few non-ground features in this area, illustrating the poor data quality of ASTER, SRTM, and ALOS DEMs in areas near the shore. The comparison of unfiltered and filtered TDX and LiDAR data showed that the filter did not improve the skewness of elevation differences much (Fig. 6a and f) or remove all non-ground features in TDX DEMs, producing a DTM that looks rougher than the DTM from filtered LiDAR data (Fig. 10).

4.3. Comparison of inundation areas from satellite DEMs and DTMs, and LiDAR DTMs

The inundation areas from ASTER, SRTM, and ALOS DEMs for a scenario of 3 m water level rise differed by > 90% from the inundation area derived from the LiDAR DTM (Table 2). The negative sign of the difference in percentage in the table indicates that inundation areas from ASTER, SRTM, and ALOS DEMs greatly underestimated the inundation extent. The difference in inundation areas for a scenario of 5 m water level was reduced but still quite large, with a range from -93% to -73%. It is obvious that inundation extent was not depicted accurately with such large errors (Fig. 11). Under this scenario, the ASTER DEM produced the largest error, incorrectly projecting almost no inundation in the coastal area around Port-au-Prince. As the magnitude of water level rise increased, the differences in inundation areas

became reduced (Table 2). The overall performances of ASTER, SRTM, and ALOS DEMs were poor, and none of the three was consistently better than the others in terms of the inundation areas for 3, 5, 10, and 15 m increases in water level.

The inundation areas from the TDX DTM produced much smaller errors, ranging from -13% for 3 m water level rise to -4% for 15 m water level rise (Table 2). The negative values of the difference percentages indicate that the TDX DTM also underestimated the inundation area as illustrated in Fig. 12. Similar to the variation in the errors of inundation areas for ASTER, SRTM, and ALOS DEMs, the errors for the TDX DTM became smaller as the magnitude of water level increased (Table 2). Errors in the areas of high, moderate, low, and extremely low risk also decreased as the magnitude of water level rise increased because the underestimates of lower and upper boundaries of a risk zone tended to cancel each other out, resulting in small errors for the calculated areas (Table 2). The comparison of TDX and LiDAR inundation contours for the most landward positions of inundation under hypothetical scenarios showed that the TDX DTM underestimated inundation extent, as indicated by MEs of -75.0 to -49.2 m and MNBs of -6.5% to -1.7% (Table 1). The SDs, RMSEs, and LE90s of the differences in the inundation contours for 3, 5, 10, and 15 m water level rises ranged from 104.4 to 144.5, 115.3–162.7, and 172.9–232.8 m. In contrast to the differences in inundation areas from TDX and LiDAR DTMs, the differences in the inundation contours did not decline with an increase in the magnitude of water level rise. As expected, the larger differences in inundation contours occurred along shoreline sections with gentle slopes, while smaller differences occurred in shoreline sections with steep slopes (Fig. 2b).

The error in inundation contours results in uncertainty in the map for potential flooding given a magnitude of storm surge and sea level rise. The effect of this error can be estimated using Eq. (10). Since the

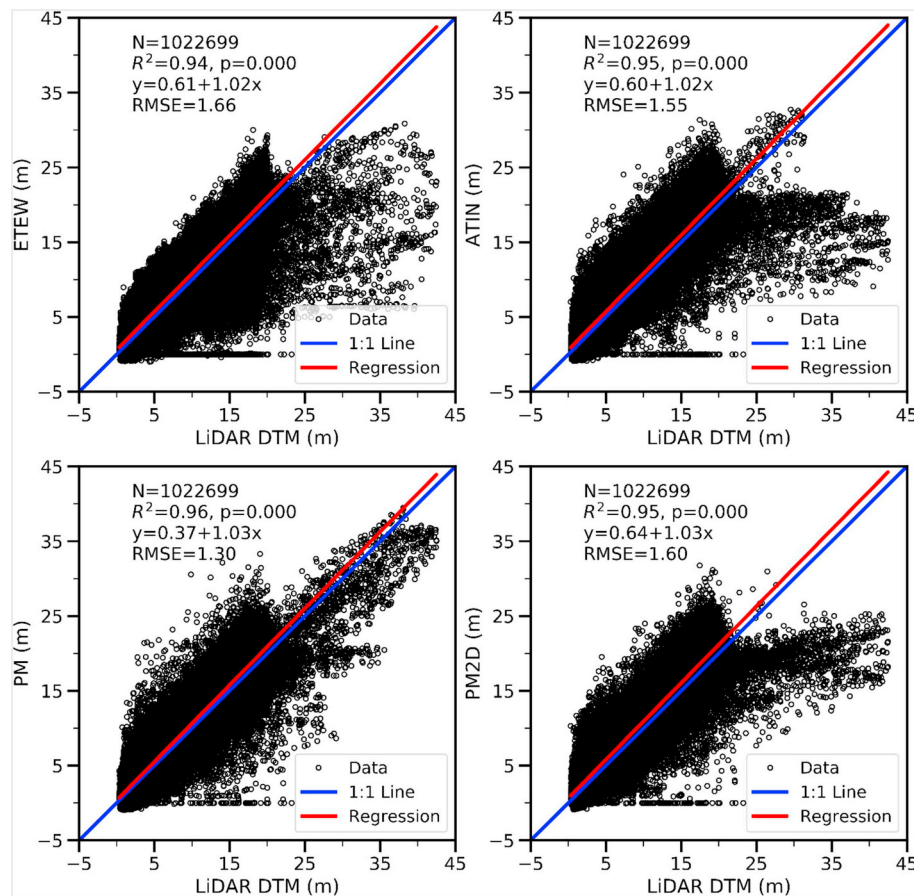


Fig. 8. Scatter plots of DTM elevations produced with EWEW, ATIN, PM, and PM2D filters versus the LiDAR DTM elevations around Port-au-Prince in Haiti.

differences between TDX and LiDAR DTMs did not follow a normal distribution (Fig. 6), the systematic offset (m) was estimated using the MD value, the random error (σ) was estimated using NAMD, δ was set to be 0.15 m, and c was set to be 2. One example of the seaward and landward extent attributable to errors between TDX and LiDAR DTMs for the 5 m inundation contour is illustrated in Fig. 12, where the difference zone between TDX and LiDAR inundation contours was bracketed by the boundaries of uncertainty.

5. Discussion

5.1. Accuracy analysis

The high accuracy of TDX DEM elevations versus GPS measurements that we observed (RMSE, 1.74 m; LE90, 3.20 m: Table 1) matches well with the accuracy assessment of TDX DEM with GPS data at a global scale (Wessel et al., 2018), who found RMSE of 1.71 m and LE90 of 2.59 m when TDX DEMs were compared with benchmark GPS measurements in areas of medium development (Table 4 in Wessel et al. (2018)). Based on aerial photographs (Fig. 1), the land cover at Pedernales, Samana, and Sanchez GPS sites assessed in our study can be categorized as areas of medium development. By removing non-ground features, TDX DTM derived by the PM filter resulted in 39% and 46% improvements in RMSE and LE90, respectively, indicating that similar filtering of TDX DEMs should be conducted whenever possible.

The RMSE and LE90 from the comparison of TDX DEM elevations with LiDAR measurements are 2.27 and 3.66 m, respectively, higher than the RMSE and LE90 from GPS measurements (Table 1). This is to be expected because the LiDAR measurements cover extensive, 150 km² areas that are occupied by many types of land cover, including marsh, forest, crop land, and low to high development. The LE90 value also

agrees with an overall LE90 of 3.49 m derived by comparing TDX DEMs with > 144 million ICESat measurements (Rizzoli et al., 2017). Similar to the GPS surveyed areas, the TDX DTM from the PM filter improved the elevation accuracy by 43% and 45% in terms of RMSE and LE90, respectively.

The inundation polygons depicted by TDX and LiDAR DTMs matched well spatially (Fig. 12) and the TDX and LiDAR inundation contours for these scenarios differed by distances that averaged < 75 m. Error measures estimated from the coastal area around Port-au-Prince, Haiti can be used to quantify the flood mapping error using TDX DTMs for the remaining areas of Hispaniola, under the assumption that the errors are likely to be similar. This is a reasonable assumption because the LiDAR surveyed area includes most coastal land cover types in Hispaniola. Transects of 1700 m length along a profile near Port-au-Prince (Fig. 9) indicated no systematic offset between elevations from TDX DEM and LiDAR DSM in open coastal areas. Several methods to map the uncertainty for coastal inundation have been proposed (Gesch, 2009; West et al., 2018). The method used in this study (i.e., Eq. (10)) resembles the method developed by Gesch (2013), except that it also considers the systematic elevation offset in the filtered TDX DEM.

It is important to conduct error analysis by comparing TDX DEM elevations with GPS and LiDAR measurements with higher accuracy. The error measures allowed us to examine whether there was an offset in TDX DEMs, and to produce lower and upper boundaries for the flood maps due to elevation uncertainty. Kinematic GPS surveying is a convenient way to collect accurate elevation data to verify TDX DEMs. The survey in this study sampled about 20 elevation points within a 30 m × 30 m square. This method captured the spatial variation in elevations within a DEM grid cell, but reduced the survey efficiency. It is probably better to survey the elevations along profiles perpendicular to contour lines, because sampling points will cover a large range of

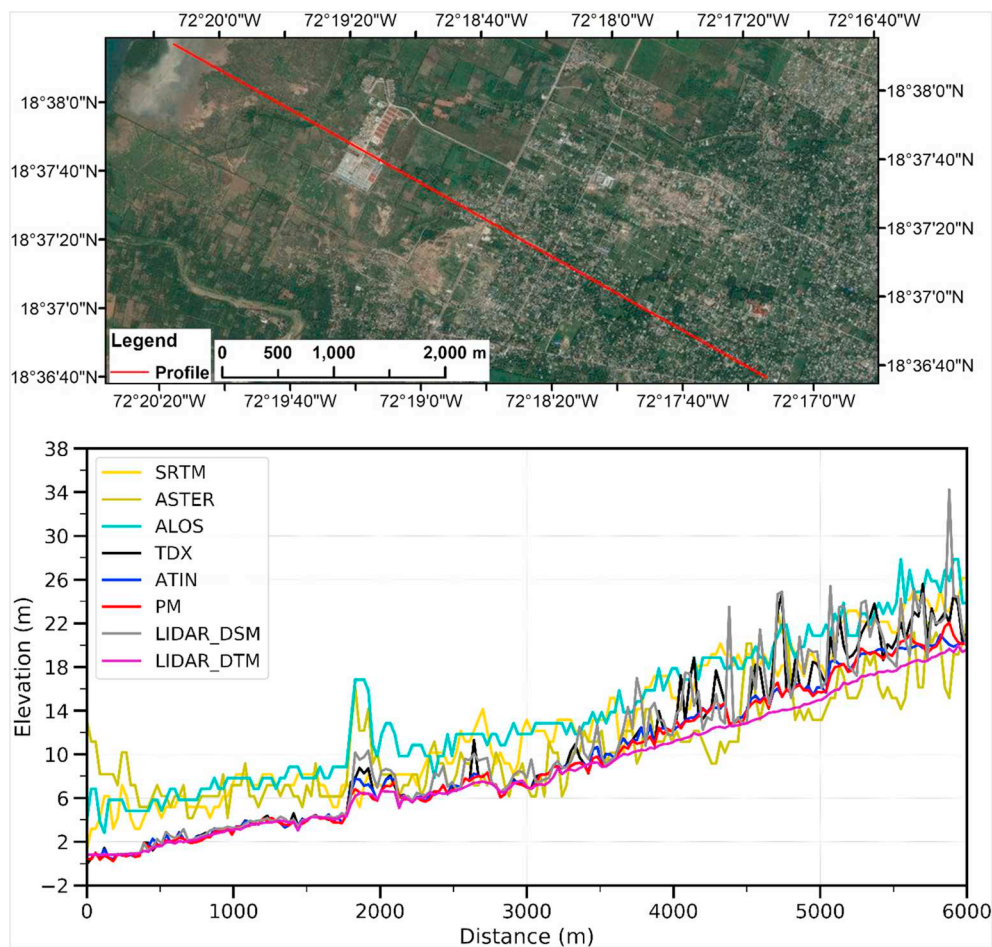


Fig. 9. Aerial photograph (upper panel) and the elevation profile (lower panel) near Port-au-Prince in Haiti. The profile starts from a location close to shore with an x coordinate of zero and extends inland.

elevations. The airborne LiDAR technology is more effective due to the large tracts of data collected, which include areas inaccessible to ground surveyors. However, the cost and time of LiDAR survey and data processing often prevent the application of LiDAR in developing countries.

In contrast to TDX DEM, ASTER, SRTM, and ALOS DEMs produced larger RMSE and LE90 errors and the performances of these three DEMs were not consistent. ALOS DEMs achieved a better accuracy than SRTM and ASTER DEMs in comparison with GPS measurements with elevations below 7 m, while at LiDAR elevations below 20 m, ASTER had a better accuracy due to a smaller offset than SRTM and ALOS DEMs. ASTER, SRTM, and ALOS DEMs generated larger discrepancies than TDX DTMs in delineation of inundation areas (Table 2) and contours (Fig. 11) for 3, 5, 10, and 15 m. Similar to elevation accuracy, none of the three was consistently better than the others in the calculation of inundation areas.

When ASTER and ALOS DEMs from the analysis of stereoscopic optical images as well as SRTM and TDX DEMs from radar were compared in pairs, both the ALOS sensor, which generated higher resolution (2.5 m) images than 15 m resolution imagery from ASTER (Abrams et al., 2010; Tadono et al., 2014), and the TDX sensors, with a longer radar baseline from two tandem satellites than the baseline from a single antenna in the space shuttle (Farr et al., 2007; Gruber et al., 2012), improve the elevation accuracy of the data. When compared on the basis of GPS measurements, both ALOS versus ASTER DEMs and TDX versus SRTM DEMs showed a better response to GPS elevation changes (Fig. 3). The comparison of DEMs with LiDAR measurements showed a similar pattern (Fig. 7), although ALOS DEM generated a

larger RMSE value than ASTER DEM due to an offset. This offset can be removed if sufficient elevation measurements (e.g. from GPS) with higher accuracy at sample sites are available.

Numerous studies in developing countries have employed open source ASTER and SRTM DEMs to map the potential flooding that will result from storm surges and sea level rise on a local scale (Aleem and Aina, 2014; Demirkesen et al., 2007; Ho et al., 2010; Kuleli, 2010; Pramanik et al., 2015; Refaat and Eldeberky, 2016). On a global scale, most studies that document potential flood risk in coastal cities or zones have used SRTM DEMs as well (Hallegatte et al., 2013; Hinkel et al., 2014; McGranahan et al., 2007). Such studies suffer the following common problems: (1) most of them did not conduct accuracy analyses, and (2) SRTM and ASTER data grossly underestimated inundation areas, especially for coastal lands below 5 m elevation. As a result, the impacted population, property, and facilities in flood-vulnerable areas were also underestimated. In the coastal area around Port-au-Prince, this underestimate was remarkable (Table 2 and Fig. 11), as the inundation areas below 5 m from SRTM and ASTER DEMs were 5 and 15 times smaller, respectively, in comparison with the LiDAR-based inundation area. Similar underestimates of inundation areas by SRTM and ASTER DEMs were also found on the local scale in Nigeria (van de Sande et al., 2012), Indonesia (Griffin et al., 2015), Poland (Walczak et al., 2016), and England (Yunus et al., 2016), and on the national level in the U.S. (Kulp and Strauss, 2016). One could argue that the RMSE in ASTER and SRTM DEMs can be improved by removing offsets through comparison of DEMs with reference data of higher accuracy. Unfortunately, the offsets may not be systematic as indicated by the scatter plot between ASTER and LiDAR DEMs in Fig. 7. Even if the offsets seem

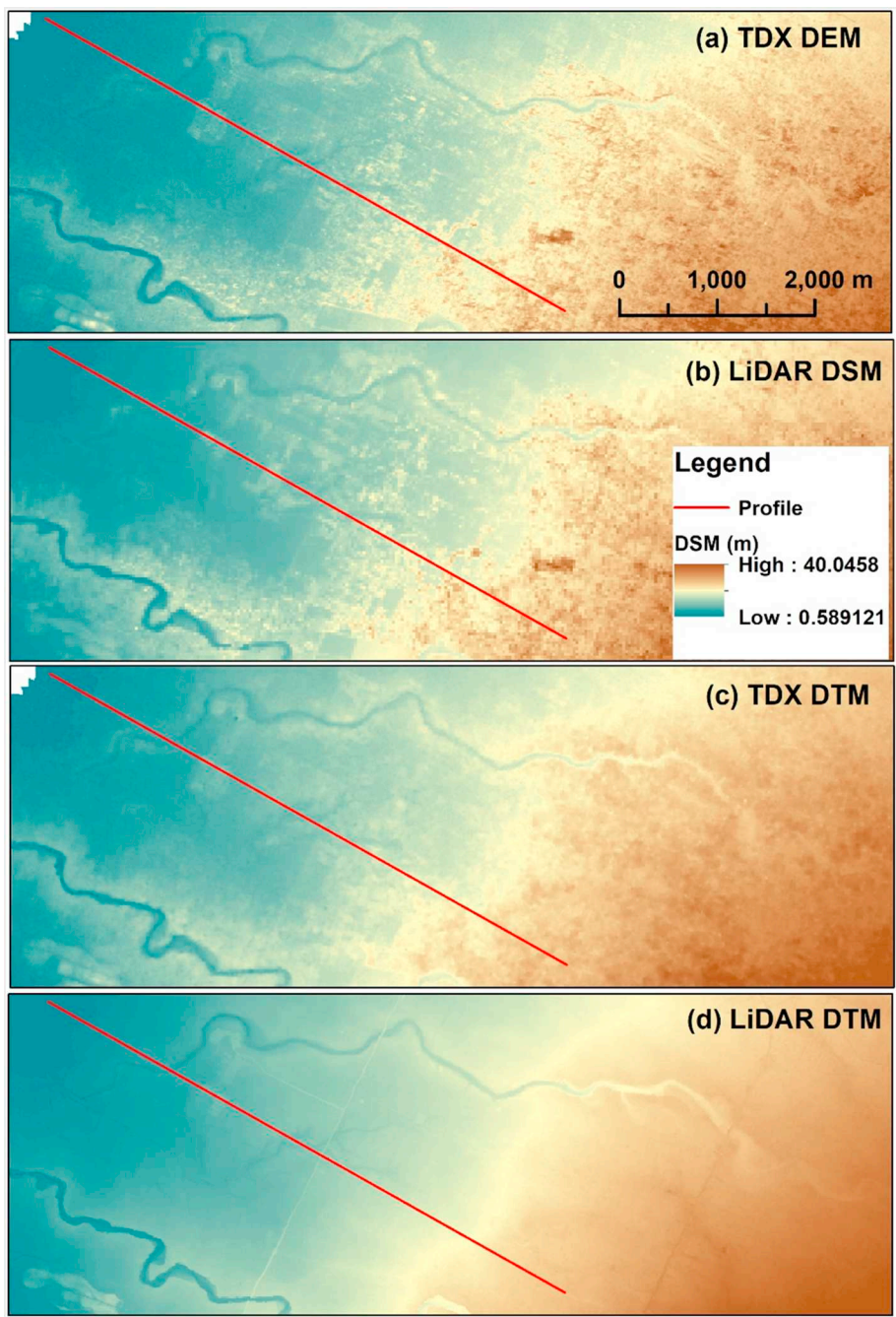


Fig. 10. TDX DEM, LiDAR DSM, TDX DTM, and LiDAR DTM for the area near Port-au-Prince in Haiti.

systematic, as indicated by scatter plots for SRTM and ALOS versus LiDAR, there is no guarantee that the offsets estimated at Port-au-Prince could be applied to places other than the study area.

In addition, inconsistent performances by ASTER, SRTM, and ALOS

DEMs in depicting inundation areas for low and high water level rise scenarios makes it difficult to select which of the three is more suitable for mapping potential coastal inundation. By contrast, the differences in estimated inundation areas around Port-au-Prince from TDX and LiDAR

Table 2

Inundation areas generated from ASTER, SRTM, and ALOS DEMs, and TDX and LiDAR DTMs for hypothetical water level rise (WLR) scenarios of 3, 5, 10, and 15 m. The TDX DTM was generated by the PM filter. The differences in percentage between the areas from ASTER, SRTM, ALOS, and TDX, and the area from LiDAR were listed in parentheses.

WLR Scenarios (m)	ASTER in km ² (%)	SRTM in km ² (%)	ALOS in km ² (%)	TDX in km ² (%)	LiDAR (km ²)	Risk class	Risk area (TDX/LiDAR, km ² /km ² /(%))
3	0.7 (−98)	2.1 (−93)	1.6 (−95)	26.0 (−13)	30.0	High	26.0/30.0 (−13)
5	3.3 (−93)	11.0 (−73)	9.0 (−82)	44.7 (−11)	50.0	Moderate	18.7/20.0 (−7)
10	68.7 (−22)	56.9 (−35)	55.1 (−38)	83.5 (−5)	88.2	Low	38.8/38.2 (2)
15	111.3 (−7)	91.2 (−24)	90.9 (−24)	114.9 (−4)	119.8	Extremely low	31.4/31.6 (−1)

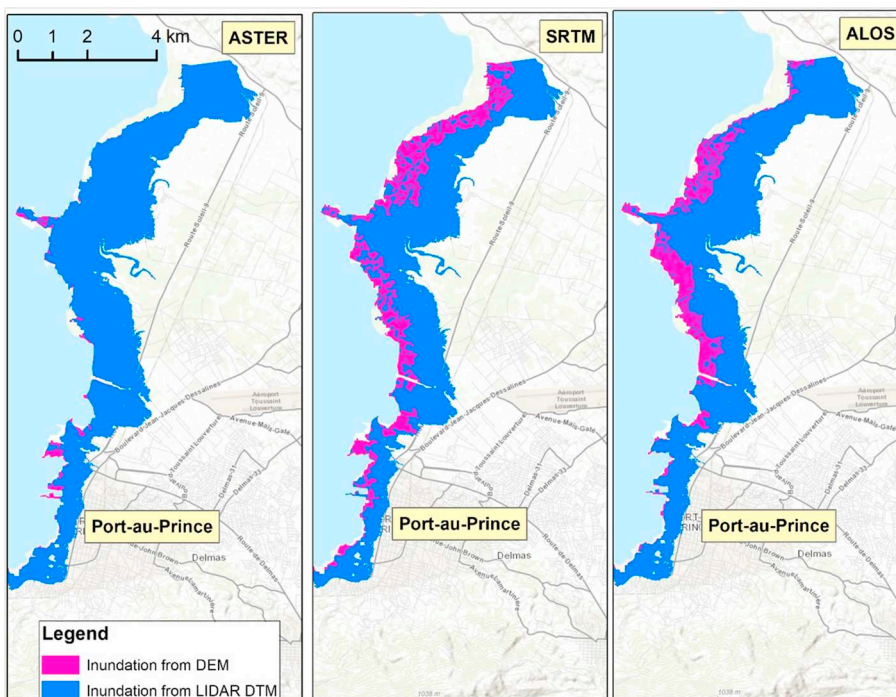


Fig. 11. The inundation areas derived from ASTER DEM, SRTM DEM, ALOS DEM and LiDAR DTM for a 5 m scenario of water level rise.

DTMs show that the TDX DTM reasonably approximates LiDAR DTM for the inundation areas below 3 m and 5 m as well as for inundation areas below 10 and 15 m (Table 2), indicating that TDX DTMs, though not as accurate as LiDAR DTMs, are practical substitutes for mapping coastal inundation. Hence, we strongly recommend utilizing TDX DEMs for global analysis of sea level rise impacts, and for local analysis in developing countries where LiDAR is not economically feasible, because the TDX DEM is the most accurate global DEM to date. It is noteworthy that the RMSE value of 1 m for TDX DTMs in the study area is

much larger than the RMSE of LiDAR DTMs. The confidence level for mapping minor floods of < 1 m using TDX DEMs is low due to this error. Therefore, caution should be taken when using TDX DTMs to map potential inundation risk solely owing to sea level rise, which, based on the IPCC projection, is about 1 m by 2100 for the worst-case scenario (Stocker et al., 2013). Gesch (2018) drew a similar conclusion by assessing the adequacy of TDX DEMs for mapping sea level rise inundation along the U.S. coasts. Another hurdle for extensive application of TDX DEMs to mapping coastal flooding in developing countries is that

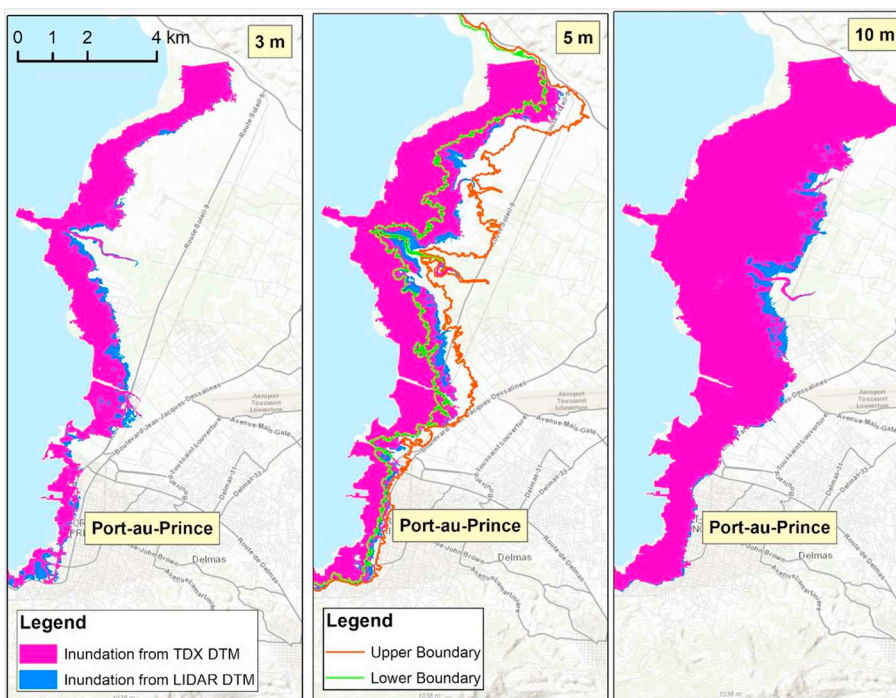


Fig. 12. Inundation areas derived from the PM-filtered TDX DTM versus those from the LiDAR DTM for 3, 5, and 10 m scenarios of water level rises. The lower and upper boundaries for the 5 m inundation area estimated using the uncertainty in the TDX data are also displayed.

TDX 12 m DEMs are not freely available, although DLR released TDX 90 m DEMs to the public in October 2018. Comparison of TDX 12 m and 90 m DEMs at Port-au-Prince, Haiti showed that 90 m DEMs captured major elevation change patterns, but smoothed out many local elevation variations because of resolution reduction. Due to this smoothing effect, the filtering of 90 m DEMs probably provides little improvement of DTM accuracy, thereby greatly increasing uncertainty in depicting inundation zones.

5.2. Filtering of TDX DEMs

It has been demonstrated that the DTMs generated by filtering and interpolating TDX DEMs resulted in approximately 40% improvement in estimates of ground elevation. Therefore, filtering methods are needed if TDX DEMs are to be used to map coastal flood hazards accurately. Among the four tested filtering methods, the PM filter using a one-dimensional structure element generated the best results because this filter effectively preserved river banks, low coastal cliffs, and gently sloping terrain features such as floodplains within the study area (Zhang et al., 2003; Zhang and Whitman, 2005). By contrast, the ETEW and ATIN methods incorrectly removed ground pixels bordering river banks, as well as low coastal cliffs where sharp elevation changes occurred. Likewise, the PM2D filter is less effective in retaining geomorphic features compared to the PM filter, due to its use of a two-dimensional square or circular structure element.

The filtering methods for LiDAR measurements can either be directly applied to the TDX DEMs (this study) or modified to fit TDX DEMs (Geiß et al., 2015; Schreyer et al., 2016) because these filters are based on a similar assumption for separation of ground and non-ground pixels. The assumption is that changes in the elevations of ground pixels are gradual and spatially correlated within a local window, while changes in elevations between ground and non-ground features are abrupt and poorly correlated. However, due to footprint sizes and data point density, TDX and LiDAR data differ remarkably in terms of their likelihood of penetrating through vegetation. LiDAR can reach the ground even in dense coastal forests such as mangroves and tropical hardwoods because of its small footprint size and high spatial measurement density (Zhang et al., 2008). By contrast, TDX measurements from the X-band radar wave cannot penetrate through dense coastal forests to reach the ground, making it impractical to separate ground elevations from non-ground elevations in these types of land cover. In heavily-built metropolitan areas, where streets are not much wider than the 12 m spatial resolution of TDX DEMs, shadow effects and the mixing of different objects in a TDX DEM pixel also prevent consistent ground measurements. In medium-developed and sparse or patchily vegetated areas, ground and non-ground features are generally separable in TDX DEMs (Rossi and Gernhardt, 2013; Schreyer and Lakes, 2016), and it is in such landscapes that TDX DEMs can provide reliable DTMs for mapping flood impacts.

Even in medium-developed or patchily vegetated areas, the improvement in identification of ground pixels by modifying the existing filtering method to fit the characteristics of TDX DEMs deserves further study. For example, the TDX sensor did not capture the ground measurements between the distances 4400 and 5000 m along a profile near Port-au-Prince (Fig. 9), resulting in an overestimate of ground elevations in the filtered data. This overestimate caused corresponding underestimates of the potential flood areas shown in Fig. 12. A possible strategy to handle this large spatial gap in ground measurements is to select high quality, well separated ground pixels from the TDX DEMs as seed points in the first step of forming the initial ground pixel set and generating an initial ground surface by interpolating ground pixels. The next step would be to iteratively search the candidate pixels and add candidates to the ground set by comparing the distances from candidate pixels to ground surface. Manual editing of automatically selected seed pixels may be needed to ensure that the seeds are reliable because the effect of the seed pixels is magnified in adding more ground pixels

through an iterative process (Zhao et al., 2016). The land cover data, especially from satellite platforms such as Sentinel that collect images with a spatial resolution similar to TDX DEMs, should be incorporated into the filtering process for selecting seed ground pixels and determining filtering parameters.

6. Conclusions

The elevation accuracy of ASTER, SRTM, ALOS, and TDX DEMs for Hispaniola were examined against > 2000 RTK GPS measurements in the Dominican Republic and 150 km² LiDAR data in Haiti to determine if these DEMs are appropriate for mapping coastal flood risk. The comparison between DEM elevations and GPS measurements below 7 m elevations showed that the TDX DEMs achieved the best accuracy, generating the smallest SD of 1.59 m, RMSE of 1.74 m, and LE90 of 3.20 m. ASTER DEMs had the lowest accuracy, generating the largest SD of 6.96 m, RMSE of 8.44 m, and LE90 of 14.29 m, while SRTM and ALOS DEMs were intermediate in accuracy with 2.58 and 1.87 m SDs, 3.82 and 2.08 m RMSEs, and 5.58 and 3.64 m LE90s, respectively. The offsets generated by non-ground features in TDX DEMs were largely removed by the ETEW, ATIN, PM, and PM2D filters. The PM filter produced the best results, reducing SD to 1.03 m, RMSE to 1.06 m, and LE90 to 1.73 m, making 39%–46% improvement over unfiltered data.

The comparison between DEM elevations and LiDAR measurements below 20 m indicated a similar pattern in accuracy from DEMs versus GPS measurements. TDX DEMs had the best accuracy, generating the smallest SD of 1.88 m, RMSE of 2.27 m, and LE90 of 3.66 m. However, SRTM DEMs produced the largest errors, with RMSE of 4.81 m, and LE90 of 7.16 m due to an offset in the data, while ASTER and ALOS DEMs generated slightly lower errors than SRTM DEMs. The error measures from DEM versus LiDAR elevations were larger than the error measures from DEM versus GPS elevations because LiDAR measurements covered a large area of 150 km², where there were multiple types of land cover including marsh, forest, crop land, and low to high development. It is better to estimate the statistical parameters for elevation differences using MD and NMAD than using ME and SD because, except for ASTER, the differences between satellite-derived and LiDAR elevations did not follow a normal distribution. The comparison of DTMs from the ETEW, ATIN, PM, and PM2D filters showed that the PM filter produced the best result, with a SD of 1.16 m, RMSE of 1.30 m, and LE90 of 2.02 m, resulting in a 43% improvement in RMSE after filtering.

The inundation areas from the TDX DTM for scenarios of 3, 5, 10, and 15 m water level rise produced errors between –13% and –4% compared to the inundation areas from LiDAR DTM. The error in estimates of inundated areas decreased as the magnitude of water level rise increased, because the area of inundation increased as water level rose, but the error of the inundation edge did not decrease. The high, moderate, low, and extremely low risk zones derived from TDX and LiDAR DTMs differed by –13%, –7%, 2%, and –1%, respectively, for a 150 km² area with elevations below 20 m. The TDX DTM underestimated the inundation extent as indicated by MEs of –75.0 to –49.2 m and SDs, RSMEs, and LE90s of the differences in inundation extent for 3, 5, 10, and 15 m water level rise ranged from 104.4 to 144.5, 115.3–162.7, and 172.9–232.8 m, respectively. Therefore, TDX DTMs provide an effective approximation of LiDAR DTMs for coastal flood mapping in the area where LiDAR data are not available. By contrast, the inundation areas from ASTER, SRTM, and ALOS DEMs for 3 and 5 m water level rise scenarios had –98% to –73% of differences compared to the inundation areas from the LiDAR DTM. The inundation areas below 5 m from SRTM and ASTER DEMs were 5 and 15 times smaller than the inundated area based on LiDAR. Among ASTER, SRTM, and ALOS DEMs, no single data source consistently performed the best in defining inundation areas for 3, 5, 10, and 15 m scenarios of water level rise. We strongly recommend that TDX DEMs be utilized to conduct both global and local analysis of sea level and storm surge impacts

in developing countries.

The DTMs generated by filtering and interpolating TDX DEMs improved the accuracy of ground elevations by about 40% along the coast near Port-au-Prince, Haiti, thereby greatly reducing the uncertainty in mapping coastal inundation caused by sea level rise and storm surges. Therefore, filtering methods must be applied to TDX DEMs to derive DTMs for accurately delineating coastal flood hazard zones. However, the effectiveness of filtering is limited by the spatial resolution of TDX DEMs for locations where dense vegetation and buildings prevent radar waves from reaching the ground. Though filtering methods employed in this study worked well for medium-developed or patchily vegetated areas, the existing filters need to be improved, or a new filter that fits the characteristics of TDX DEMs needs to be developed to generate better DTMs in the future.

Acknowledgements

This work was supported by “Development of an Integrated Coastal Inundation Forecast Demonstration System in the Caribbean Region – Pilot Project for the Dominican Republic and Haiti” sponsored by the United States Agency for International Development (USAID) and National Oceanic and Atmospheric Administration. The German Aerospace Center provided TanDEM-X DEM data for Hispaniola through the project “Developing Hurricane Storm Surge Planning and Forecasting Capabilities for Haiti and the Dominican Republic Using TanDEM-X DEMs” (Proposal ID: DEM_HYDR0550). We thank the USAID’s Office of U.S. Foreign Disaster Assistance (USAID/OFDA) for their support to conduct the RTK GPS survey in Hispaniola, through the Florida International University’s Disaster Risk Reduction Program. We are also grateful to Dr. Dar Roberts, Associate Editor and three anonymous reviewers for providing valuable comments which have been very helpful in improving the manuscript.

References

- Abrams, M., Bailey, B., Tsu, H., Hato, M., 2010. The aster global dem. *Photogramm. Eng. Remote Sensing* 76, 344–348.
- Aleem, K.F., Aina, Y.A., 2014. Using SRTM and GDEM2 data for assessing vulnerability to coastal flooding due to sea level rise in Lagos: a comparative study. *FUTY J. Environ.* 8, 53–64.
- Axelsson, P., 2000. DEM generation from laser scanner data using adaptive TIN models. *Int. Arch. Photogramm. Remote Sens.* 33, 110–117.
- Bamber, J.L., Riva, R.E.M., Vermeersen, B.L.A., Lebrocq, A.M., 2009. Reassessment of the potential of the West Antarctic ice sheet. *Science* 324, 901–904. <https://doi.org/10.1126/science.1169335>. (80-).
- Boulton, S.J., Stokes, M., 2018. Which DEM is best for analyzing fluvial landscape development in mountainous terrains? *Geomorphology* 310, 168–187.
- Cui, Z., Zhang, K., Zhang, C., Yan, J., Chen, S.C., 2013. A GUI based LIDAR data processing system for model generation and mapping. In: *Proceedings of the 1st ACM SIGSPATIAL International Workshop on MapInteraction*. ACM, Orlando, pp. 40–43.
- Davis, J., 2002. *Statistics and Data Analysis in Geology*, 3rd ed. John Wiley & Sons, Inc, New York.
- Demirkesen, A.C., Evrendilek, F., Berberoglu, S., Kilic, S., 2007. Coastal flood risk analysis using Landsat-7 ETM+ imagery and SRTM DEM: a case study of Izmir, Turkey. *Environ. Monit. Assess.* 131, 293–300.
- Demirkesen, A.C., Evrendilek, F., Berberoglu, S., 2008. Quantifying coastal inundation vulnerability of Turkey to sea-level rise. *Environ. Monit. Assess.* 138, 101–106.
- Farr, T.G., Rosen, P.A., Caro, E., Crippen, R., Duren, R., Hensley, S., Kobrick, M., Paller, M., Rodriguez, E., Roth, L., 2007. The shuttle radar topography mission. *Rev. Geophys.* 45. <https://doi.org/10.1029/2005RG000183>.
- Franzen, D.W., Clay, D., Shanahan, J.F., 2011. Collecting and analyzing soil spatial information using kriging and inverse distance. In: Clay, D.E., Shanahan, J.F. (Eds.), *GIS Appl. Agric. Nutr. Manag. Energy Effic.* Taylor Fr, New York, NY, USA, pp. 61–80.
- Geiß, C., Wurm, M., Breunig, M., Felbier, A., Taubenböck, H., 2015. Normalization of TanDEM-X DSM data in urban environments with morphological filters. *IEEE Trans. Geosci. Remote Sens.* 53, 4348–4362.
- Gesch, D.B., 2009. Analysis of lidar elevation data for improved identification and delineation of lands vulnerable to sea-level rise. *J. Coast. Res.* 49–58.
- Gesch, D.B., 2013. Consideration of vertical uncertainty in elevation-based sea-level rise assessments: Mobile Bay, Alabama case study. *J. Coast. Res.* 63, 197–210.
- Gesch, D.B., 2018. Best practices for elevation-based assessments of sea-level rise and coastal flooding exposure. *Front. Earth Sci.* 6, 230.
- Griffin, J., Latief, H., Kongko, W., Harig, S., Horspool, N., Hanung, R., Rojali, A., Maher, N., Fuchs, A., Hossen, J., 2015. An evaluation of onshore digital elevation models for modeling tsunami inundation zones. *Front. Earth Sci.* 3, 32.
- Gruber, A., Wessel, B., Huber, M., Roth, A., 2012. Operational TanDEM-X DEM calibration and first validation results. *ISPRS J. Photogramm. Remote Sens.* 73, 924–2716.
- Hallegatte, S., Green, C., Nicholls, R.J., Corfee-Morlot, J., 2013. Future flood losses in major coastal cities. *Nat. Clim. Chang.* 3, 802.
- Hinkel, J., Lincke, D., Vafeidis, A.T., Perrette, M., Nicholls, R.J., Tol, R.S.J., Marzeion, B., Fettweis, X., Ionescu, C., Levermann, A., 2014. Coastal flood damage and adaptation costs under 21st century sea-level rise. *Proc. Natl. Acad. Sci.* 111, 3292–3297.
- Ho, L.T.K., Umitzu, M., Yamaguchi, Y., 2010. Flood hazard mapping by satellite images and SRTM DEM in the Vu Gia–Thu Bon alluvial plain, Central Vietnam. *Int. Arch. Photogramm. Remote. Sens. Spat. Inf. Sci.* 38, 275–280.
- Höhle, J., Höhle, M., 2009. Accuracy assessment of digital elevation models by means of robust statistical methods. *ISPRS J. Photogramm. Remote Sens.* 64, 398–406.
- ITRF, 2013. ITRS and WGS84. <ftp://itrf.eng.ign.fr/pub/itrf/WGS84.TXT>, Accessed date: 3 November 2018.
- Knutson, T.R., McBride, J.L., Chan, J., Emanuel, K., Holland, G., Landsea, C., Held, I., Kossin, J.P., Srivastava, A.K., Sugi, M., 2010. Tropical cyclones and climate change. *Nat. Geosci.* 3, 157.
- Komar, P.D., 1998. *Beach Processes and Sedimentation*. Prentice Hall, Upper Saddle River, New Jersey.
- Krieger, G., Moreira, A., Fiedler, H., Hajnsek, I., Werner, M., Younis, M., Zink, M., 2007. TanDEM-X: a satellite formation for high-resolution SAR interferometry. *IEEE Trans. Geosci. Remote Sens.* 45, 3317–3341.
- Krivoruchko, K., 2012. Empirical Bayesian Kriging. *ArcUser Fall 2012*. pp. 6–10.
- Kuleli, T., 2010. City-based risk assessment of sea level rise using topographic and census data for the Turkish coastal zone. *Estuar. Coasts* 33, 640–651.
- Kulp, S., Strauss, B.H., 2016. Global DEM errors underpredict coastal vulnerability to sea level rise and flooding. *Front. Earth Sci.* 4, 36.
- Leatherman, S.P., Clow, B., 1983. UMD shoreline mapping project. *IEEE Geosci. Remote Sens. Soc. Newsl.* 22, 5–8.
- McGranahan, G., Balk, D., Anderson, B., 2007. The rising tide: assessing the risks of climate change and human settlements in low elevation coastal zones. *Environ. Urban.* 19, 17–37.
- Mirzaei, R., Sakizadeh, M., 2016. Comparison of interpolation methods for the estimation of groundwater contamination in Andimeshk-Shush Plain, Southwest of Iran. *Environ. Sci. Pollut. Res.* 23, 2758–2769.
- Neumann, B., Vafeidis, A.T., Zimmermann, J., Nicholls, R.J., 2015. Future coastal population growth and exposure to sea-level rise and coastal flooding: a global assessment. *PLoS One* 10, e0118571. <https://doi.org/10.1371/journal.pone.0118571>.
- Nicholls, R.J., Marinova, N., Lowe, J.A., Brown, S., Vellinga, P., De Gusmao, D., Hinkel, J., Tol, R.S.J., 2011. Sea-level rise and its possible impacts given a ‘beyond 4 C world’ in the twenty-first century. *Philos. Trans. R. Soc. London A Math. Phys. Eng. Sci.* 369, 161–181.
- Pavlis, N.K., Holmes, S.A., Kenyon, S.C., Factor, J.K., 2012. The development and evaluation of the earth gravitational model 2008 (EGM2008). *J. Geophys. Res. Solid Earth* 117. <https://doi.org/10.1029/2011JB008916>.
- Pramanik, M.K., Biswas, S.S., Mukherjee, T., Roy, A.K., Pal, R., Mondal, B., 2015. Sea level rise and coastal vulnerability along the eastern coast of India through geospatial technologies. *J. Geophys. Remote Sens.* 4, 145. <https://doi.org/10.4172/2469-4134.1000145>.
- Refaat, M.M., Eldeberky, Y., 2016. Assessment of coastal inundation due to sea-level rise along the Mediterranean Coast of Egypt. *Mar. Geod.* 39, 290–304.
- Rizzoli, P., Martone, M., Gonzalez, C., Wecklich, C., Tridon, D.B., Bräutigam, B., Bachmann, M., Schulze, D., Fritz, T., Huber, M., 2017. Generation and performance assessment of the global TanDEM-X digital elevation model. *ISPRS J. Photogramm. Remote Sens.* 132, 119–139.
- Roberts, J.D., Voss, J.D., Knight, B., 2014. The association of ambient air pollution and physical inactivity in the United States. *PLoS One* 9. <https://doi.org/10.1371/journal.pone.0090143>.
- Robertson, Q., Dunkin, L., Dong, Z., Wozencraft, J., Zhang, K., 2018. Florida and US east coast beach change metrics derived from LIDAR data utilizing ArcGIS Python based tools. In: Botero, C.M., Cervantes, O., Finkl, C.W. (Eds.), *Beach Management Tools-Concepts, Methodologies and Case Studies*. Springer International Publishing AG, Cham, pp. 239–258.
- Rodriguez, M.O.C., Barba, D.C., 2009. The Hispaniola fluvial system and its morpho-structural context. *Phys. Geogr.* 30, 453–478.
- Rodriguez, E., Morris, C.S., Belz, J.E., 2006. A global assessment of the SRTM performance. *Photogramm. Eng. Remote. Sens.* 72, 249–260.
- Rossi, C., Gernhardt, S., 2013. Urban DEM generation, analysis and enhancements using TanDEM-X. *ISPRS J. Photogramm. Remote Sens.* 85, 120–131.
- Schreyer, J., Lakes, T., 2016. Deriving and evaluating city-wide vegetation heights from a TanDEM-X DEM. *Remote Sens.* 8, 940.
- Schreyer, J., Geiß, C., Lakes, T., 2016. TanDEM-X for large-area modeling of urban vegetation height: evidence from Berlin, Germany. *IEEE J. Sel. Top. Appl. Earth Obs. Remote Sens.* 9, 1876–1887.
- Shan, J., Toth, C.K., 2008. *Topographic Laser Ranging and Scanning: Principles and Processing*. CRC Press, Boca Raton.
- Stocker, T.F., Qin, D., Plattner, G.K., Tignor, M., Allen, S.K., Boschung, J., Nauels, A., Xia, Y., Bex, V., Midgley, P.M., 2013. *Climate change 2013: the physical science basis: Working Group I contribution to the Fifth assessment report of the Intergovernmental Panel on Climate Change*. Cambridge University Press.
- Sweet, W.V., Kopp, R.E., Weaver, C.P., Obeysekera, J., Horton, R.M., Thieler, E.R., Zervas, C., 2017. *Global and Regional Sea Level Rise Scenarios for the United States*. National Oceanic and Atmospheric Administration, Silver Spring.
- Tachikawa, T., Hato, M., Kaku, M., Iwasaki, A., 2011a. Characteristics of ASTER GDEM version 2. In: *Geoscience and Remote Sensing Symposium (IGARSS)*, 2011 IEEE International. IEEE, Vancouver, pp. 3657–3660.

- Tachikawa, T., Kaku, M., Iwasaki, A., Gesch, D., Oimoen, M., Zhang, Z., Danielson, J., Krieger, T., Curtis, B., Haase, J., NASA, 2011b. ASTER Global Digital Elevation Model Version 2—Summary of Validation Results. https://ssl.jspacsystems.or.jp/ersdac/GDEM/ver2Validation/Summary_GDEM2_validation_report_final.pdf, Accessed date: 3 November 2018.
- Tadono, T., Ishida, H., Oda, F., Naito, S., Minakawa, K., Iwamoto, H., 2014. Precise global DEM generation by ALOS PRISM. *ISPRS Ann. Photogramm. Remote Sens. Spat. Inf. Sci.* 2, 71.
- Tadono, T., Nagai, H., Ishida, H., Oda, F., Naito, S., Minakawa, K., Iwamoto, H., 2016. Generation of the 30 m-mesh global digital surface model by ALOS PRISM. *Int. Arch. Photogramm. Remote. Sens. Spat. Inf. Sci.* 41.
- Takaku, J., Tadono, T., 2009. PRISM on-orbit geometric calibration and DSM performance. *IEEE Trans. Geosci. Remote Sens.* 47, 4060–4073.
- Takaku, J., Tadono, T., 2017. Quality updates of 'AW3D' global DSM generated from ALOS PRISM, in: *Geoscience and remote sensing symposium (IGARSS)*. In: 2017 IEEE International. IEEE, Fort Worth, pp. 5666–5669.
- Takaku, J., Tadono, T., Tsutsui, K., 2014. Generation of high resolution global DSM from ALOS PRISM. *Int. Arch. Photogramm. Remote. Sens. Spat. Inf. Sci.* 40, 243.
- Takaku, J., Tadono, T., Tsutsui, K., Ichikawa, M., 2016. Validation of "AW3D" global DSM generated from ALOS PRISM. *ISPRS Ann. Photogramm. Remote Sens. Spat. Inf. Sci.* 3, 25.
- United Nations, 2017. *World population prospects: 2017 revision, data booklet. ST/ESA/SER.A/401*. <https://population.un.org/wpp/Publications/>, Accessed date: 3 November 2018.
- Van Aardt, J.A.N., McKeown, D., Faulring, J., Raqueño, N., Casterline, M., Renschler, C., Eguchi, R., Messinger, D., Krzaczek, R., Cavillia, S., 2011. Geospatial disaster response during the Haiti earthquake: a case study spanning airborne deployment, data collection, transfer, processing, and dissemination. *Photogramm. Eng. Remote Sensing* 77, 943–952.
- van de Sande, B., Larsen, J., Hoyng, C., 2012. Sensitivity of coastal flood risk assessments to digital elevation models. *Water* 4, 568–579.
- Walczak, Z., Sojka, M., Wróżyński, R., Laks, I., 2016. Estimation of polder retention capacity based on ASTER, SRTM and LIDAR DEMs: the case of Majdany Polder (West Poland). *Water* 8, 230.
- Wessel, B., 2016. *TanDEM-X Ground Segment-DEM Products Specification Document*. German Space Center.
- Wessel, B., Huber, M., Wohlfart, C., Marschalk, U., Kosmann, D., Roth, A., 2018. Accuracy assessment of the global TanDEM-X digital elevation model with GPS data. *ISPRS J. Photogramm. Remote Sens.* 1–12.
- West, H., Horswell, M., Quinn, N., 2018. Exploring the sensitivity of coastal inundation modelling to DEM vertical error. *Int. J. Geogr. Inf. Sci.* 32, 1172–1193.
- Wilson, J.S., Brothers, T.S., Marcano, E.J., 2001. Remote sensing of spatial and temporal vegetation dynamics in Hispaniola: a comparison of Haiti and the Dominican Republic. *Geocarto Int* 16, 7–18.
- Wolf, P.R., Dewitt, B.A., Wilkinson, B.E., 2000. *Elements of Photogrammetry: With Applications in GIS*. McGraw-Hill, New York.
- Yunus, A.P., Avtar, R., Kraines, S., Yamamuro, M., Lindberg, F., Grimmond, C.S.B., 2016. Uncertainties in tidally adjusted estimates of sea level rise flooding (bathtub model) for the Greater London. *Remote Sens.* 8, 366.
- Zhang, K., 2007. *Airborne LiDAR data processing and analysis tools*. In: *AGU Fall Meeting Abstracts*, . <http://adsabs.harvard.edu/abs/2007AGUFM.H52E..01Z>, Accessed date: 8 November 2018.
- Zhang, K., 2011. Analysis of non-linear inundation from sea-level rise using LIDAR data: a case study for South Florida. *Clim. Chang.* 106, 537–565.
- Zhang, K., Robertson, W., 2001. Historical shoreline mapping and analysis with metric mapping. In: *Coastal GeoTools'01. Proceedings of the 2nd Biennial Coastal GeoTools Conference*, . http://coastalgeotools.org/wp-content/uploads/GeoTools2011_program.pdf, Accessed date: 8 November 2018.
- Zhang, K., Whitman, D., 2005. Comparison of three algorithms for filtering airborne lidar data. *Photogramm. Eng. Remote. Sens.* 71, 313–324.
- Zhang, K., Chen, S.-C., Whitman, D., Shyu, M.-L., Yan, J., Zhang, C., 2003. A progressive morphological filter for removing nonground measurements from airborne LIDAR data. *IEEE Trans. Geosci. Remote Sens.* 41, 872–882.
- Zhang, K., Simard, M., Ross, M., Rivera-Monroy, V.H., Houle, P., Ruiz, P., Twilley, R.R., Whelan, K., 2008. Airborne laser scanning quantification of disturbances from hurricanes and lightning strikes to mangrove forests in Everglades National Park, USA. *Sensors* 8, 2262–2292.
- Zhang, K., Dittmar, J., Ross, M., Bergh, C., 2011. Assessment of sea level rise impacts on human population and real property in the Florida Keys. *Clim. Chang.* 107, 129–146.
- Zhao, X., Guo, Q., Su, Y., Xue, B., 2016. Improved progressive TIN densification filtering algorithm for airborne LiDAR data in forested areas. *ISPRS J. Photogramm. Remote Sens.* 117, 79–91.
- Zink, M., Bachmann, M., Brautigam, B., Fritz, T., Hajnsek, I., Moreira, A., Wessel, B., Krieger, G., 2014. TanDEM-X: the new global DEM takes shape. *IEEE Geosci. Remote Sens. Mag.* 2, 8–23.